

Paleoceanography and Paleoclimatology



RESEARCH ARTICLE

10.1029/2023PA004773

Spatial and Temporal Patterns in Petrogenic Organic Carbon Mobilization During the Paleocene-Eocene Thermal Maximum

Special Section:

Illuminating a Warmer World:
 Insights from the Paleogene

E. H. Hollingsworth¹ , F. J. Elling^{2,3} , M. P. S. Badger^{4,5} , R. D. Pancost⁴ , A. J. Dickson⁶ ,
 R. L. Rees-Owen⁴, N. M. Papadomanolaki^{7,8} , A. Pearson², A. Sluijs⁷ , K. H. Freeman⁹ ,
 A. A. Baczyński⁹ , G. L. Foster¹, J. H. Whiteside^{1,10}, and G. N. Inglis¹ 

Key Points:

- We assess spatial and temporal patterns in petrogenic organic carbon (OC_{petro}) mobilization during the Paleocene-Eocene Thermal Maximum
- Evidence for enhanced OC_{petro} mobilization in the subtropics and mid-latitudes, likely due to an increase in extreme rainfall events
- OC_{petro} mobilization remained elevated during the recovery phase of the Paleocene-Eocene Thermal Maximum

Supporting Information:

Supporting Information may be found in the online version of this article.

Correspondence to:

G. N. Inglis and E. H. Hollingsworth,
Gordon.inglis@soton.ac.uk;
e.hollingsworth@soton.ac.uk

Citation:

Hollingsworth, E. H., Elling, F. J., Badger, M. P. S., Pancost, R. D., Dickson, A. J., Rees-Owen, R. L., et al. (2024). Spatial and temporal patterns in petrogenic organic carbon mobilization during the Paleocene-Eocene Thermal Maximum. *Paleoceanography and Paleoclimatology*, 39, e2023PA004773. <https://doi.org/10.1029/2023PA004773>

Received 27 SEP 2023
 Accepted 16 JAN 2024

Author Contributions:

Conceptualization: E. H. Hollingsworth, G. N. Inglis
Funding acquisition: G. N. Inglis
Investigation: E. H. Hollingsworth, F. J. Elling, M. P. S. Badger, A. J. Dickson, R. L. Rees-Owen, N. M. Papadomanolaki, G. N. Inglis

© 2024. The Authors.

This is an open access article under the terms of the [Creative Commons Attribution License](https://creativecommons.org/licenses/by/4.0/), which permits use, distribution and reproduction in any medium, provided the original work is properly cited.

¹School of Ocean and Earth Science, University of Southampton, Southampton, UK, ²Department of Earth and Planetary Sciences, Harvard University, Cambridge, MA, USA, ³Leibniz-Laboratory for Radiometric Dating and Isotope Research, Christian-Albrechts, University of Kiel, Kiel, Germany, ⁴Organic Geochemistry Unit, School of Earth Sciences, School of Chemistry, University of Bristol, Bristol, UK, ⁵School of Environment, Earth and Ecosystem Sciences, The Open University, Milton Keynes, UK, ⁶Centre of Climate, Ocean and Atmosphere, Department of Earth Sciences, Royal Holloway University of London, Surrey, UK, ⁷Department of Earth Sciences, Utrecht University, Utrecht, The Netherlands, ⁸Institute of Geology and Paleontology, University of Münster, Münster, Germany, ⁹Department of Geosciences, The Pennsylvania State University, University Park, PA, USA, ¹⁰Now at Department of Earth and Environmental Sciences, San Diego State University, San Diego, CA, USA

Abstract The Paleocene-Eocene Thermal Maximum (PETM) was a transient global warming event and is recognized in the geologic record by a prolonged negative carbon isotope excursion (CIE). The onset of the CIE was due to a rapid influx of ¹³C-depleted carbon into the ocean-atmosphere system. However, the mechanisms required to sustain the negative CIE remains unclear. Enhanced mobilization and oxidation of petrogenic organic carbon (OC_{petro}) has been invoked to explain elevated atmospheric carbon dioxide concentrations after the onset of the CIE. However, existing evidence is limited to the mid-latitudes and subtropics. Here, we determine whether: (a) enhanced mobilization and subsequent burial of OC_{petro} in marine sediments was a global phenomenon; and (b) whether it occurred throughout the PETM. To achieve this, we utilize a lipid biomarker approach to trace and quantify OC_{petro} burial in a global compilation of PETM-aged shallow marine sites ($n = 7$, including five new sites). Our results confirm that OC_{petro} mass accumulation rates (MARs) increased within the subtropics and mid-latitudes during the PETM, consistent with evidence of higher physical erosion rates and intense episodic rainfall events. High-latitude sites do not exhibit drastic changes in the source of organic carbon during the PETM and OC_{petro} MARs increase slightly or remain stable, perhaps due a more stable hydrological regime. Crucially, we also demonstrate that OC_{petro} MARs remained elevated during the recovery phase of the PETM. Although OC_{petro} oxidation was likely an important positive feedback mechanism throughout the PETM, we show that this feedback was both spatially and temporally variable.

Plain Language Summary The Paleocene-Eocene Thermal Maximum (PETM) was the most severe global warming event of the last 66 million years and was caused by the rapid release of greenhouse gases into the atmosphere. However, scientists have been unable to determine why the PETM lasted for >100,000 years. Here, we test whether CO₂ released from the erosion, transport, and oxidation of ancient rock-derived (or petrogenic) organic carbon can explain the long duration of the PETM. We also aim to identify if this occurred globally and/or throughout the PETM. We achieve this by looking at biomarkers (molecular fossils) and use this approach to “fingerprint” the input of petrogenic organic carbon into the marine realm. Our results suggest enhanced transport of petrogenic organic carbon was restricted to the subtropics and mid-latitudes, with limited changes in the high-latitudes. We also find evidence for erosion and transport of petrogenic organic carbon throughout the PETM. Therefore, this process likely contributed to increasing atmospheric CO₂ levels and may have been an important positive feedback mechanism in past and future warm climates.

1. Introduction

Climate and tectonics have modulated the flux of carbon to and from terrestrial reservoirs over geological timescales. Early studies predominantly focused on understanding the role of inorganic carbon, for example, carbon dioxide (CO₂) released from solid Earth degassing versus CO₂ drawdown from silicate weathering (e.g., Berner

Project Administration: E. H. Hollingsworth, G. N. Inglis
Resources: F. J. Elling, A. Pearson
Supervision: G. L. Foster, J. H. Whiteside, G. N. Inglis
Visualization: E. H. Hollingsworth
Writing – original draft: E. H. Hollingsworth
Writing – review & editing: E. H. Hollingsworth, F. J. Elling, M. P. S. Badger, R. D. Pancost, A. J. Dickson, R. L. Rees-Owen, N. M. Papadomanolaki, A. Pearson, A. Sluijs, K. H. Freeman, A. A. Baczynski, G. L. Foster, J. H. Whiteside, G. N. Inglis

& Caldeira, 1997; Berner et al., 1983; Walker et al., 1981). However, the past two decades have highlighted the importance of the terrestrial organic carbon cycle as a climate feedback mechanism (Hilton & West, 2020). Whether it acts as a positive or negative feedback mechanism largely depends on whether the organic carbon (OC) is “biospheric” (OC_{bio}), representing relatively recent thermally immature organic carbon (10^2 – 10^4 years old; e.g., vegetation and soils), or “petrogenic” (OC_{petro}), representing ancient rock-derived and thermally mature organic carbon ($>10^6$ years old; e.g., organic carbon-rich shales). Erosion, mobilization, and the subsequent burial of OC_{bio} in marine sediments helps to sequester CO_2 (Berhe et al., 2007; Stallard, 1998). In contrast, exhumation and oxidation of OC_{petro} during lateral transport from land-to-sea can release CO_2 (Petsch et al., 2000). In modern settings, up to ~90% of OC_{petro} is oxidized in large catchments such as the Amazon and Himalayan range (e.g., Bouchez et al., 2010; Galy et al., 2008), whereas a lower proportion (~10%–40%) of OC_{petro} is oxidized in mountain basins with steep rivers (e.g., Hilton et al., 2011, 2014). Crucially, regardless of individual catchment dynamics, OC_{petro} has the potential to be oxidized and increase atmospheric CO_2 concentrations.

Several studies have quantified the mobilization and burial of OC_{petro} in modern systems (e.g., Blair et al., 2003; Clark et al., 2017, 2022; T. I. Eglinton et al., 2021 and references therein; Galy et al., 2007, 2015 and references therein; Hilton & West, 2020; Hilton et al., 2010, 2011 and references therein; Smith et al., 2013) and Holocene sediments (e.g., Hilton et al., 2015; Kao et al., 2008, 2014). These studies show that erosion and transport of OC_{petro} is largely controlled by a combination of geomorphic and climate processes (e.g., T. I. Eglinton et al., 2021; Hilton, 2017). For example, extreme rainfall events can trigger bedrock landslides (e.g., Hilton et al., 2008) and/or create deeply incised gullies (e.g., Leithold et al., 2006), both of which can expose OC_{petro} to oxidation. However, clastic sediments from hyperpycnal flows and turbidites can act to enhance the preservation of OC_{petro} (e.g., Bouchez et al., 2014; Hilton et al., 2011). As climate model simulations indicate an intensification of the hydrological cycle in response to rising atmospheric CO_2 levels and global temperatures (Lee et al., 2021), the delivery of OC_{petro} to the oceans will likely be enhanced in the future. However, such predictions are based on present-day observations and/or past climate states that span a lower-than-modern atmospheric CO_2 values (e.g., Hilton & West, 2020; Kao et al., 2008).

The geologic record enables investigations into high CO_2 states of the past, providing unique insights into how terrestrial carbon cycle processes may operate in the future. Many studies have focused on the Paleocene-Eocene Thermal Maximum (PETM; ~56 million years ago) (McInerney & Wing, 2011), a transient carbon cycle perturbation characterized by global warming (~4–6°C; Inglis et al., 2020; Tierney et al., 2022) and an intensified hydrological cycle (Carmichael et al., 2017 and references therein). The PETM is identified in the geologic record by a negative carbon isotope excursion (CIE) ($-4 \pm 0.4\%$; Elling et al., 2019). The onset of the PETM is on the order-of-millennia (Kirtland Turner, 2018; Zeebe et al., 2014) and is followed by sustained low and stable carbon isotope ($\delta^{13}C$) values for ~94–170 thousand years (Kyr) (Zeebe & Lourens, 2019), referred to as the “body” of the CIE (Bowen et al., 2006). The body is then followed by a long recovery of ~50–120 Kyr (Bowen, 2013; Murphy et al., 2010; Zeebe et al., 2009), which is further divided into Phase I (initial rapid rise in $\delta^{13}C$) and Phase II (final gradual rise in $\delta^{13}C$) (Röhl et al., 2007).

The onset of the CIE was the result of a rapid influx of ^{13}C -depleted carbon from one or more reservoirs outside the active global exogenic carbon pool (Dickens et al., 1997). Proposed reservoirs include submarine methane hydrates (Dickens, 2011; Dickens et al., 1995), terrestrial organic carbon (Bowen, 2013; Deconto et al., 2012; Kurtz et al., 2003), and volcanic carbon related to the North Atlantic Igneous Province (Gutjahr et al., 2017; Jones et al., 2019; Storey et al., 2007; Svensen et al., 2004). Less explored are the mechanisms responsible for the prolonged body of the CIE. This feature requires continual input of ^{13}C -depleted carbon (e.g., Zeebe et al., 2009), thus several feedback mechanisms (either acting individually or in combination) have been proposed. This includes a slow dissociation of oceanic methane hydrates (Zeebe, 2013), pulsed releases of thermogenic methane from vent complexes (e.g., Frieling et al., 2016; Kirtland Turner, 2018), and/or “leaky” terrestrial organic carbon reservoirs (Bowen, 2013). Alternatively, recent work suggests that CO_2 released from OC_{petro} oxidation could explain the extended body of the CIE (Lyons et al., 2019). This theory is based on evidence for an order-of-magnitude increase in the delivery of OC_{petro} to the oceans, ~10–20 Kyr after the onset of the PETM. However, this study was limited to the mid-latitudes (Atlantic Coastal Plain) and subtropics (Tanzania), and therefore may not be globally representative. It is also unclear whether enhanced mobilization of OC_{petro} was a persistent feature throughout the PETM or whether it was restricted to the body interval.

Here, we use lipid biomarker thermal maturity ratios to fingerprint OC_{petro} burial in a global compilation of PETM-aged shallow marine sites ($n = 7$, including five new sites). Lipid biomarkers undergo various structural alterations with increasing thermal maturity (e.g., defunctionalization, isomerization, catagenesis, and aromatization; Peters

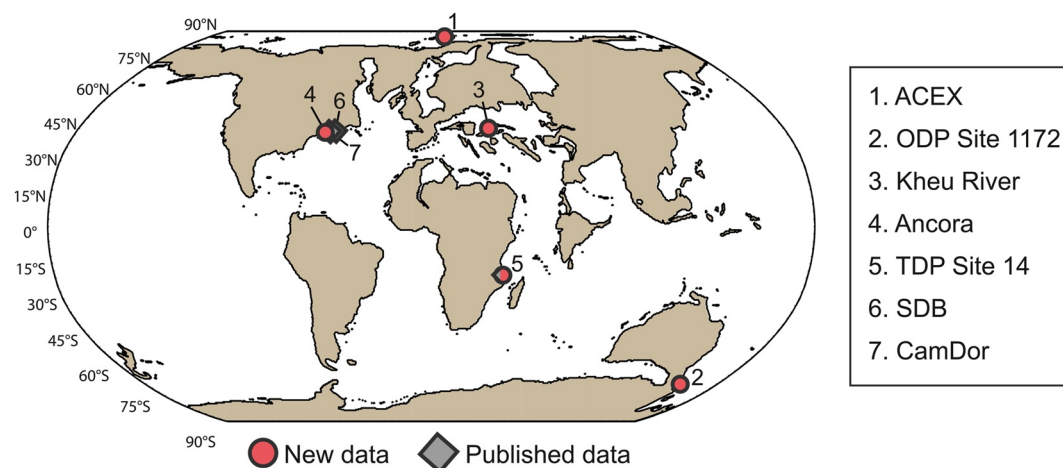


Figure 1. Location of sites with new data (1–5) and published data (5–7). Paleogeographic reconstructions of 56 million years ago, adapted from Carmichael et al. (2017).

et al., 2005) and thus, can be used to assess the proportion of OC_{petro} in marine sediments (Lyons et al., 2019). We focus on thermally immature, shallow marine sediments as they are “hotspots” for terrestrial organic carbon input (Bianchi et al., 2018). We quantify OC_{petro} burial fluxes before and during the PETM, using a two endmember mixing model. Overall, we aim to determine whether: (a) enhanced mobilization and subsequent burial of OC_{petro} in the ocean was a global phenomenon; and (b) whether it occurred throughout the PETM.

2. Methods

2.1. Data Compilation

New *n*-alkane- and/or hopane-based thermal maturity ratios were acquired from the following PETM-aged shallow marine sites: the International Ocean Drilling Program Expedition 302 Site M0004A (or the Arctic Coring Expedition; **ACEX**); the Ocean Drilling Program Site 1172 Hole D (**ODP Site 1172**); **Kheu River**; ODP Leg 174AX Ancora Site Hole A/B (**Ancora**); and the Tanzania Drilling Project Site 14 Hole A (**TDP Site 14**) (Figure 1). Additional information (e.g., paleodepth) and a brief description of the lithology for each site can be found within Table S1 and Text S1 in Supporting Information S1, respectively. We also compile *n*-alkane- and/or hopane-based thermal maturity ratios from the following published PETM-aged shallow marine sites: TDP Site 14 (Carmichael et al., 2017; Handley et al., 2012); South Dover Bridge (**SDB**) (Lyons et al., 2019); and Cambridge-Dorchester Airport (**CamDor**) (Lyons et al., 2019) (Figure 1). Other published biomarker records are available for PETM-aged shallow marine sites, however these sequences are dominated by autochthonous OC_{petro} and show evidence for post-depositional diagenesis (Cui et al., 2021; Handley et al., 2011).

2.2. Organic Geochemistry

For this study, samples from ACEX ($n = 94$), ODP Site 1172 ($n = 41$), and Ancora ($n = 42$) were freeze dried, homogenized, and extracted using a MARS5 microwave-assisted extraction system, with: (a) dichloromethane:methanol (DCM:MeOH; 1:1, v:v); (b) DCM:MeOH (9:1, v:v); and (c) DCM, at Harvard University (see Elling et al., 2019). Each solvent mixture was heated for 30 min to 100°C, followed by a hold time of 20 min. The extracts from the three steps were combined into a total lipid extract (TLE) and further divided into five fractions (following Polik et al. (2018)). At the University of Southampton, extracted copper was added to the apolar fractions for 24 hr to remove elemental sulfur. The apolar fractions were then analyzed using a ThermoFisher Trace 1310 gas chromatograph (GC) coupled to a Thermo TSQ8000 Triple Quadrupole mass spectrometer (MS). Helium was used as the carrier gas and separation was achieved with DB-5 column (30 m × 0.25 mm i.d., 0.25 μm film thickness). The GC oven program started at 70°C for 1 min, increased to 130°C at 20°C min⁻¹, followed by 300°C at 4°C min⁻¹, which was then held for 20 min. MS scanning occurred between mass-to-charge ratio (m/z) 50 to 650 Da, and an ionization energy of 70 eV. Compound identification was based on retention times, fragmentation patterns, comparison to an in-house standard, and library matches.

Kheu River samples ($n = 39$) were extracted at the University of Bristol by ultrasonically homogenized samples sequentially with DCM, DCM:MeOH (1:1, v:v), and MeOH. Elemental sulfur was removed from the combined TLE using activated copper turnings. An activated silica column with saturated ammonia in chloroform and chloroform:acetic acid (100:1, v:v) was used to separate the neutral and acid fraction, respectively. The apolar fraction was split from the neutral fraction by eluting with hexane:DCM (9:1, v:v) via separation on an alumina column. The apolar fractions were then analyzed at the University of Bristol on a Thermoquest Finnigan Trace GC interfaced with a Thermoquest Finnigan Trace MS. The GC was fitted with a fused capillary column (50 m \times 0.32 mm i.d.) and the carrier gas was helium. The samples were suspended in ethyl acetate and injected at 70°C. The temperature program increased to 130°C (20°C min⁻¹), then 300°C (4°C min⁻¹), and finally remained isothermal for 20 min. The MS operated with an electron ionization source at 70 eV, scanning over m/z ranges of 50–850 Da. The compounds were integrated on the total ion chromatogram (TIC).

Additional samples ($n = 12$) from TDP Site 14 were homogenized and extracted at the University of Bristol. Extractions were achieved via Soxhlet apparatus overnight, using DCM:MeOH (2:1 v:v). The TLE was suspended in hexane:DCM (9:1, v:v) and separated by alumina column chromatography. Co-eluting compounds and/or unresolved complex mixtures were reduced with urea adduction (following Pancost et al., 2008). Elemental sulfur was removed using extracted copper turnings. The apolar fractions were analyzed at the University of Bristol on the same GC-MS as used for Kheu River. The GC was fitted with a CPsil-5CB column (Agilent Technologies, dimethylpolysiloxane stationary phase) and the carrier gas was helium. The samples were injected in ethyl acetate at 70°C. The temperature program increased to 130°C (20°C min⁻¹), then 300°C (4°C min⁻¹), and finally held for 25 min. The MS operated with an electron ionization source at 70 eV, scanning over m/z ranges of 50–850 Da. The compounds were integrated on the TIC or using the appropriate mass fragment (e.g., m/z 191).

2.3. Lipid Biomarker Proxies

2.3.1. *n*-Alkane-Based Thermal Maturity Ratios

Modern plants and sediments contain long-chain *n*-alkanes with an odd-over-even preference (G. Eglinton & Hamilton, 1967), however this is progressively lost during diagenesis. The shift away from a dominance of long-chain *n*-alkanes with an odd-over-even predominance is captured by the carbon preference index (CPI) (Bush & McNerney, 2013). Modern sediments exhibit high CPI values (>3–30), indicating relatively unaltered thermally immature organic matter (Diefendorf & Freimuth, 2017). In contrast, mature organic matter (e.g., coal and oil) exhibits low CPI values (~1). CPI values <1 are less common, and typify low-maturity source rocks from carbonates or hypersaline environments. In this study, sites with extensive post-depositional diagenesis were excluded, such that CPI values closer to 1 likely suggests input of allochthonous thermally mature organic matter (e.g., OC_{petro}). Here, we use the equation as originally defined by Bray and Evans (1961):

$$\text{CPI} = \frac{1}{2} \left[\left(\frac{\sum_{\text{odd}} (C_{25-31})}{\sum_{\text{even}} (C_{26-32})} \right) + \left(\frac{\sum_{\text{odd}} (C_{27-33})}{\sum_{\text{even}} (C_{26-32})} \right) \right] \quad (1)$$

2.3.2. Hopane-Based Thermal Maturity Ratios

Hopanes are the diagenetic products of biohopanoids, which are produced by a wide diversity of bacteria and consequently ubiquitous in a range of environments (Kusch & Rush, 2022). The ratios between different hopanes and their various stereoisomers have long been utilized as a thermal maturity proxy in the field of petroleum geochemistry (e.g., Farrimond et al., 1998; Mackenzie et al., 1980). Most of the hopane-based thermal maturity ratios used in this study are normalized (with the exception of Equation 4). Values indicating high thermal maturity likely suggests allochthonous older material (e.g., pre-PETM-aged OC_{petro}), as sites with post-depositional diagenesis were excluded from this study. We use a multi-ratio approach as each ratio corresponds to different stages of maturity relative to the oil window (i.e., from early diagenesis to the generation of oil), thus enabling insight on the degree of thermal maturation (Figure S1 in Supporting Information S1). However, hopane distributions also vary depending on the lithofacies and/or depositional environment (Peters et al., 2005). Therefore, without knowledge of the source rock at each locality, comparison between the sites should be undertaken with caution.

With the exception of *Frankia* spp. (Rosa-Putra et al., 2001), all bacteria synthesize hopanoids with a 17 β , 21 β configuration. However, this changes to a more stable $\beta\alpha$ and then $\alpha\beta$ configuration during early diagenesis and

then peak oil generation, respectively (Farrimond et al., 1998; Mackenzie et al., 1980). The shift from $\beta\beta$ to $\alpha\beta$ is expressed via the following equation (sometimes referred in literature as “hopanoid isomerization”):

$$\alpha\beta/(\alpha\beta + \beta\beta) \quad (2)$$

Higher thermal maturity is marked by values closer to 1. This equation is applied to the hopanes that contained both isomers (i.e., mostly C_{29-31} hopanes). However, caution should be taken when interpreting sediments with input from peats, as C_{31} $\alpha\beta$ isomers dominate the hopane distribution within acidic wetland environments (Inglis et al., 2018).

The shift from $\beta\alpha$ (also referred to as moretane; M) to the more stable $\alpha\beta$ (also referred to as hopane; H) is assessed via the following equation (sometimes referred in literature as “moretane/hopane ratio”):

$$\beta\alpha/(\beta\alpha + \alpha\beta) \quad (3)$$

This equation is applied to the most commonly used C_{30} hopane (e.g., French et al., 2012), as well as the less commonly used C_{29} hopane (Peters et al., 2005). Values closer to ~ 0 indicate higher thermal maturity and oil generation.

The C_{29} $\alpha\beta$ hopane (also referred to as norhopane; N) is more thermally stable than C_{30} $\alpha\beta$ hopane. This is assessed via the following equation (sometimes referred in literature as “norhopane/hopane ratio”):

$$C_{29} \alpha\beta/C_{30} \alpha\beta \quad (4)$$

As well as a thermal maturity proxy, this ratio has been utilized to differentiate between anoxic carbonate and/or marl source rocks (>1) versus clay-rich source rocks (<1) (Peters et al., 2005).

Toward the early stages of oil generation, there is a change in stereochemistry at the C-22 position, from the biologically favored R configuration to a near equal mix of R and S (Farrimond et al., 1998; Mackenzie et al., 1980; Peters et al., 2005). This is expressed via the following equation (sometimes referred in literature as “homohopane isomerization”):

$$S/(S + R) \quad (5)$$

This equation uses C_{31-35} hopanes (also referred to as homohopanes) and approaches maximum (equilibrium) values of ~ 0.6 as thermal maturity increases and oil is generated.

At the late stage of oil generation, C_{27} hopanes shift in the position of a D-ring methyl group, from C-18 ($17\alpha(H),22,29,30$ -trisorhopane; T_m) to C-17 ($18\alpha(H),22,29,30$ -trisorneohopane; T_s) (Farrimond et al., 1998; Peters et al., 2005). This is expressed via the following equation:

$$T_s/(T_s + T_m) \quad (6)$$

T_m refers to maturable (less stable), whereas T_s denotes stable. Values closer to 1 indicate higher thermal maturity, although the oxicity of the depositional environment also has a notable influence (Peters et al., 2005).

2.4. Two-Endmember Mixing Model

The fraction of OC_{petro} (f_{petro}) was calculated for each hopane-based thermal maturity ratio (X_{mix} ; Table 1), following the two endmember mixing model from Lyons et al. (2019):

$$X_{\text{mix}} = f_{\text{petro}} \times X_{\text{petro}} + (1 - f_{\text{petro}}) \times X_{\text{background}} \quad (7)$$

where $X_{\text{background}}$ and X_{petro} is the defined immature and mature endmembers, respectively. The endmembers for C_{31-35} $S/(S + R)$ ratio follow the definitions in Lyons et al. (2019), where $X_{\text{background}}$ is the contemporaneous carbon value of 0 and X_{petro} is the most thermally mature value of 0.6. The endmembers for C_{29-30} $\beta\alpha/(\beta\alpha + \alpha\beta)$ ratio also follow the definitions in Lyons et al. (2019), where $X_{\text{background}}$ is 1 and X_{petro} is 0. For this study, the endmembers of the $\alpha\beta/(\alpha\beta + \beta\beta)$ ratio was defined as 0 for $X_{\text{background}}$ and 1 for X_{petro} . Note that C_{29} $\alpha\beta/C_{30}$ $\alpha\beta$ and $T_s/(T_s + T_m)$ ratios were excluded due to their strong dependence on the source rock and/or depositional environment (Peters et al., 2005).

Table 1
Variables Used to Calculate f_{petro}

Site	X_{mix}	LSR (cm Kyr ⁻¹)				Organic carbon content (%) references
		Pre-PETM	Core PETM	Recovery PETM		
				Phase I	Phase II	
ACEX ^a	$C_{30-31} \alpha\beta/(\alpha\beta + \beta\beta)$	1		Min: 3.8	Max: 6.2	TOC Elling et al. (2019)
	$C_{31} S/(S + R)$					
	$C_{30} \beta\alpha/(\beta\alpha + \alpha\beta)$					
ODP Site 1172 ^b	$C_{30-31} \alpha\beta/(\alpha\beta + \beta\beta)$	0.57	Min: 0.4 Max: 0.5	Not available		C_{org} Papadomanolaki et al. (2022)
	$C_{31} S/(S + R)$					
	$C_{30} \beta\alpha/(\beta\alpha + \alpha\beta)$					
Kheu River ^c	$C_{29-31} \alpha\beta/(\alpha\beta + \beta\beta)$	0.3		1.9		C_{org} Dickson et al. (2014)
	$C_{29-30} \beta\alpha/(\beta\alpha + \alpha\beta)$					
Ancora ^d	$C_{30-31} \alpha\beta/(\alpha\beta + \beta\beta)$	0.8	11.2 and 4.3	1.3	8.4	TOC Elling et al. (2019)
	$C_{31} S/(S + R)$					
	$C_{30} \beta\alpha/(\beta\alpha + \alpha\beta)$					
TDP Site 14 ^e	$C_{29-31} \alpha\beta/(\alpha\beta + \beta\beta)$	Min: 0.5	Min: 3.5	NA		C_{org} Aze et al. (2014)
	$C_{31-35} S/(S + R)$	Max: 2	Max: 14			
	$C_{29-30} \beta\alpha/(\beta\alpha + \alpha\beta)$					
SDB ^f	$C_{31} S/(S + R)$	Min: 1.03	14	21.3	21.3	TOC Lyons et al. (2019)
	$C_{29} \beta\alpha/(\beta\alpha + \alpha\beta)^{\S}$	Max: 2.4				
CamDor ^f	$C_{29} \beta\alpha/(\beta\alpha + \alpha\beta)^{\S}$	Min: 1.03		14		TOC Lyons et al. (2019)
	$C_{31-32} S/(S + R)^{\S}$	Max: 2.4				

Note. a–f References for LSR.

^aSluijs, Röhl, et al. (2008). ^bSluijs et al. (2011). ^cJohn et al. (2008). ^dStassen et al. (2012). ^eLyons et al. (2019). ^fDoubrawa et al. (2022). [§] f_{petro} calculated in Lyons et al. (2019).

2.5. Mass Accumulation Rates

The mass accumulation rate (MAR; in gC cm² Kyr⁻¹) of OC_{petro} was calculated for all the new and published f_{petro} data, following Lyons et al. (2019):

$$\text{MAR} = \text{LSR} \times \rho \times f_{\text{petro}} \times \frac{\text{TOC}}{100} \quad (8)$$

where LSR is the linear sedimentation rate (cm Kyr⁻¹), ρ is the dry bulk density (g cm⁻³), and TOC is the total organic carbon (TOC) or C_{org} (%) (see Table 1). As published bulk density values are only available for one site (ODP Site 1172), a constant ρ value of 1.8 g cm⁻³ was assumed across all the sites (following Dunkley Jones et al., 2018). However, we acknowledge that changes in dry bulk density may influence absolute MARs, especially in sites with major lithological changes (see Text S1 in Supporting Information S1). The TOC values and LSR were acquired for each location from published studies (Table 1). C_{org} records from ODP Site 1172 (Papadomanolaki et al., 2022) and TDP Site 14 (Aze et al., 2014) were linearly interpolated to match the depths of the biomarker data, using R Package Astrochron (Meyers, 2014). LSR estimates were obtained (where possible) for three key time intervals: (i) pre-PETM (Paleocene); (ii) the “core” (onset and body of the CIE) of the PETM; (iii) and the recovery of the PETM (see Text S1 in Supporting Information S1). This was available for all the sites with the exception of ODP Site 1172, which lacks the recovery interval. Note that the recovery at Ancora and SDB were further divided into: (iiia) Phase I; and (iiib) Phase II. Kheu River does not have LSR data, thus estimates were taken from the nearby Aktumsuk section (Uzbekistan; John et al., 2008). Both Kheu River and Aktumsuk comprises shallow marine deposits that exhibits TOC values from ~0.1% pre-PETM to a maximum of ~8.5% during the PETM (Bolle et al., 2000; Dickson et al., 2014). Similarly, LSRs from within the core interval of SDB was assumed to be the same for the entire PETM section at CamDor (following Lyons et al., 2019).

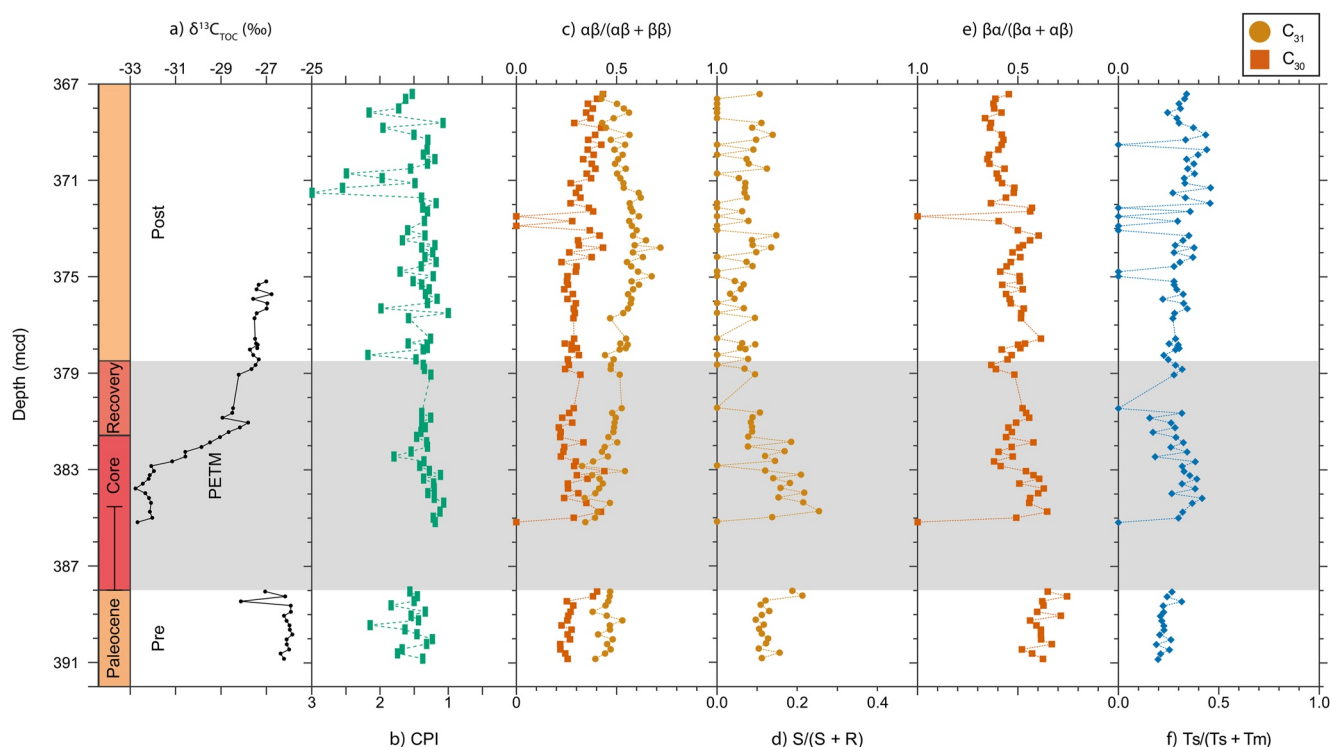


Figure 2. Thermal maturity ratios at ACEX. Note some of the axis (CPI and $\beta\alpha/(\beta\alpha + \alpha\beta)$) are reversed to reflect increasing thermal maturity toward the right. (a) bulk sediment $\delta^{13}\text{C}$ of total organic carbon ($\delta^{13}\text{C}_{\text{TOC}}$) (Elling et al., 2019), (b) CPI (this study), (c) $\alpha\beta/(\alpha\beta + \beta\beta)$ ratios (this study), (d) $S/(S + R)$ ratio (this study), (e) $\beta\alpha/(\beta\alpha + \alpha\beta)$ ratio (this study), and (f) $T_s/(T_s + T_m)$ ratio (this study). The PETM interval (including the core and recovery) is highlighted by gray shading, and a core gap is present from ~ 388 to 384.5 mcd (Sluijs et al., 2006).

3. Results

3.1. Thermal Maturity Ratios

3.1.1. ACEX

The apolar fraction contains short- (C_{15-19}), mid- (C_{21-25}), and long- (C_{27-33}) chain *n*-alkanes, and $\text{C}_{27}\text{--}\text{C}_{32}$ hopanes (including $\alpha\beta$, $\beta\alpha$, and $\beta\beta$ isomers). Both the CPI (ranging from ~ 1 to 3; Figure 2b) and hopane-based thermal maturity ratios exhibit relatively stable trends throughout the sequence, suggesting that the organic carbon source did not distinctly change. Note that potential information may be missing due poor core recovery between ~ 388 and 384.5 mcd (Sluijs et al., 2006). However, C_{30} $\alpha\beta/(\alpha\beta + \beta\beta)$ (Figure 2c), C_{31} $S/(S + R)$ (Figure 2d), and $T_s/(T_s + T_m)$ (Figure 2f) values slightly increase (i.e., higher thermal maturity) between pre-PETM and the core of the PETM, by an average of 0.01, 0.01, and 0.08, respectively. These indices then decline during the recovery interval. C_{31} $\alpha\beta/(\alpha\beta + \beta\beta)$ and C_{30} $\beta\alpha/(\beta\alpha + \alpha\beta)$ ratios (Figure 2c) exhibit the opposite trend, with lower thermal maturity during the core interval and the C_{30} $\beta\alpha/(\beta\alpha + \alpha\beta)$ ratio (Figure 2e) continuing to decline into the recovery of the PETM.

3.1.2. ODP Site 1172

The apolar fraction contains $\text{C}_{16}\text{--}\text{C}_{34}$ *n*-alkanes and the CPI has a mean value of 2.8. Samples with $\text{CPI} > 3$ (i.e., relatively low thermal maturity), are mostly constrained to the pre-PETM interval (Figure 3b). Hopanes range from C_{27} to C_{32} (including $\alpha\beta$, $\beta\alpha$, and $\beta\beta$ isomers), and the thermal maturity ratios exhibit a relatively stable trend throughout the sequence. However, the C_{31} $S/(S + R)$ ratio slightly increases by 0.09 during the core interval and into the recovery of the PETM (Figure 3d), suggesting potential input of thermally mature organic carbon. C_{30} $\alpha\beta/(\alpha\beta + \beta\beta)$ (Figure 3c), C_{31} $\alpha\beta/(\alpha\beta + \beta\beta)$ (Figure 3c), and C_{30} $\beta\alpha/(\beta\alpha + \alpha\beta)$ (Figure 3e) values exhibit the opposite behavior, shifting toward relatively thermally immature values during the core of the PETM, by an average of 0.19, 0.22, and 0.07, respectively. During the recovery, C_{30} $\alpha\beta/(\alpha\beta + \beta\beta)$ (Figure 3c), C_{31} $\alpha\beta/(\alpha\beta + \beta\beta)$ (Figure 3c), and C_{30} $\beta\alpha/(\beta\alpha + \alpha\beta)$ (Figure 3e) ratios return to relatively more thermally mature values.

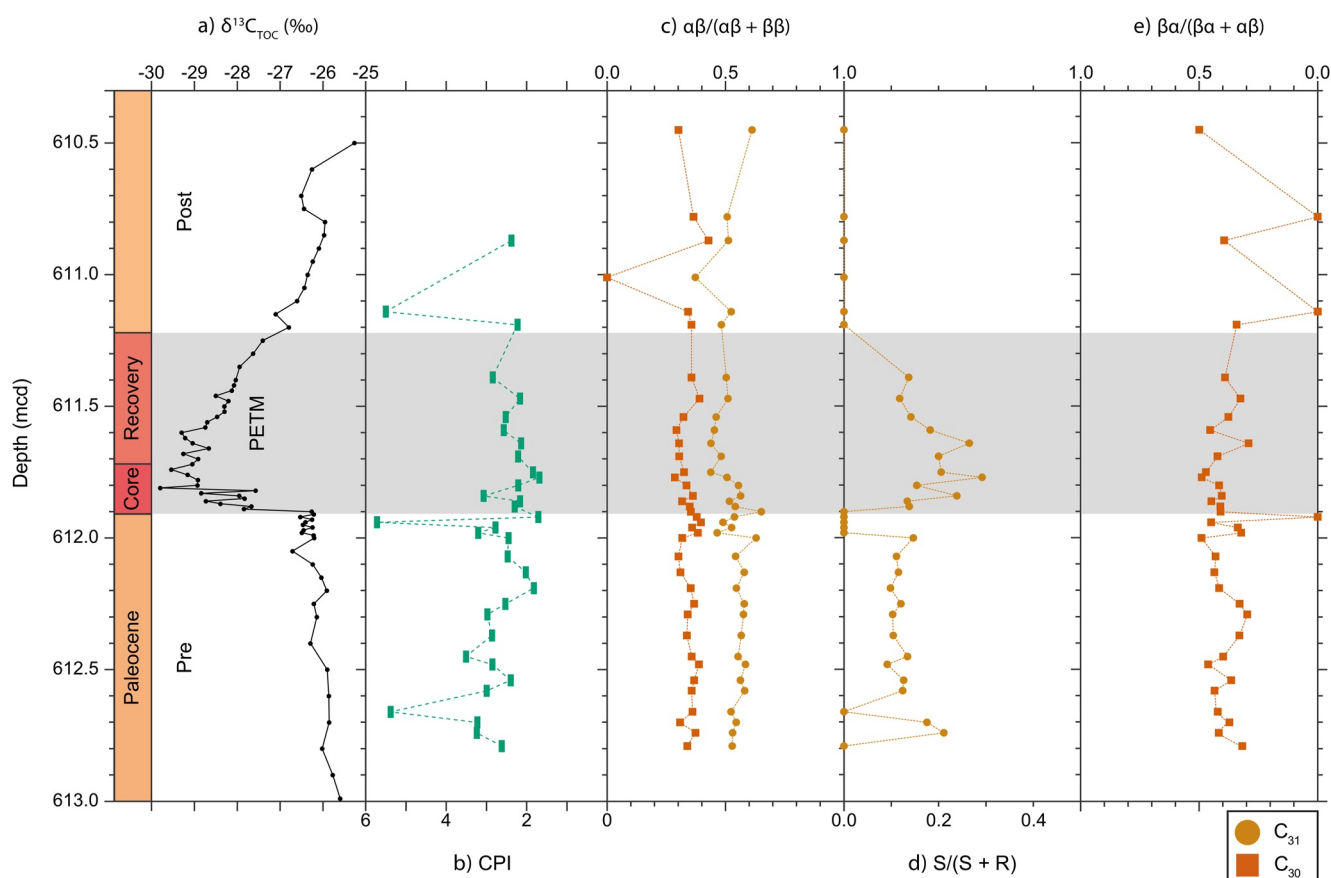


Figure 3. Thermal maturity ratios at ODP Site 1172. Note some of the axis (CPI and $\beta\alpha/(\beta\alpha + \alpha\beta)$) are reversed to reflect increasing thermal maturity toward the right. (a) bulk sediment $\delta^{13}\text{C}$ of total organic carbon ($\delta^{13}\text{C}_{\text{TOC}}$) (Sluijs et al., 2011), (b) CPI (this study), (c) $\alpha\beta/(\alpha\beta + \beta\beta)$ ratios (this study), (d) $S/(S + R)$ ratio (this study), and (e) $\beta\alpha/(\beta\alpha + \alpha\beta)$ ratio (this study). The PETM interval (including the core and recovery) is highlighted by gray shading.

3.1.3. Kheu River

C_{16} – C_{35} *n*-alkanes were identified in the apolar fraction, in addition to C_{27} – C_{31} hopanes (including $\alpha\beta$, $\beta\alpha$, and $\beta\beta$ isomers). Prior to the PETM and during the recovery, the CPI drops below 1 (Figure 4b), which may suggest input of low-maturity source rocks from carbonates or hypersaline environments. The CPI also oscillate drastically between ~ 1 and ~ 3 within the lower depths of the core of the PETM (~ 0 – 50 cm; Figure 4b). This section of high variability is also reflected in the C_{29} $\alpha\beta/\text{C}_{30}$ $\alpha\beta$ (Figure 4d) and C_{29} $\beta\alpha/(\beta\alpha + \alpha\beta)$ (Figure 4e) ratios, suggesting rapid changes in the organic carbon source. However, it may also represent greater sampling resolution within the PETM. Overall, the average of all the thermal maturity ratios exhibit lower thermal maturity during the core interval. In addition, the C_{29} $\alpha\beta/\text{C}_{30}$ $\alpha\beta$ ratio present values >1 during the PETM (Figure 4d), potentially indicating input from a clay-rich source rock. With the exception of $T_s/(T_s + T_m)$ (Figure 4f), all of the ratios increase in higher thermal maturity during the recovery to either higher than pre-PETM (i.e., C_{29} $\alpha\beta/(\text{C}_{29}$ $\alpha\beta + \text{C}_{30}$ $\alpha\beta)$ and C_{29-30} $\beta\alpha/(\beta\alpha + \alpha\beta)$ ratios) or near pre-PETM values (i.e., C_{29-31} $\alpha\beta/(\alpha\beta + \beta\beta)$ ratio).

3.1.4. Ancora

The apolar fraction contains C_{15} – C_{34} *n*-alkanes and C_{27} to C_{31} hopanes (including $\alpha\beta$, $\beta\alpha$, and $\beta\beta$ isomers). CPI ranges from 1 to 2.2 and is similar during the pre-PETM and PETM interval (Figure 5b). Similarly, C_{30-31} $\alpha\beta/(\alpha\beta + \beta\beta)$ values remain relatively constant, albeit exhibiting a very slight decline by an average of 0.01–0.03 (i.e., decreasing thermal maturity; Figure 5c). On the other hand, C_{31} $S/(S + R)$ (Figure 5d) and C_{30} $\beta\alpha/(\beta\alpha + \alpha\beta)$ (Figure 5e) values peak toward higher thermal maturity during the core of the PETM, reaching a maximum of 0.38 and 0.04, respectively. C_{31} $S/(S + R)$ values exhibit a drastic shift during the PETM (Figure 5d) and there is near equal mix of 22S and 22R isomers, suggesting potential transient input of thermally mature organic carbon. Changes in the C_{31} $S/(S + R)$ ratio and C_{30} $\beta\alpha/(\beta\alpha + \alpha\beta)$ ratio do not occur synchronously, instead C_{31} $S/(S + R)$ values lag behind by ~ 1.5 mcd.

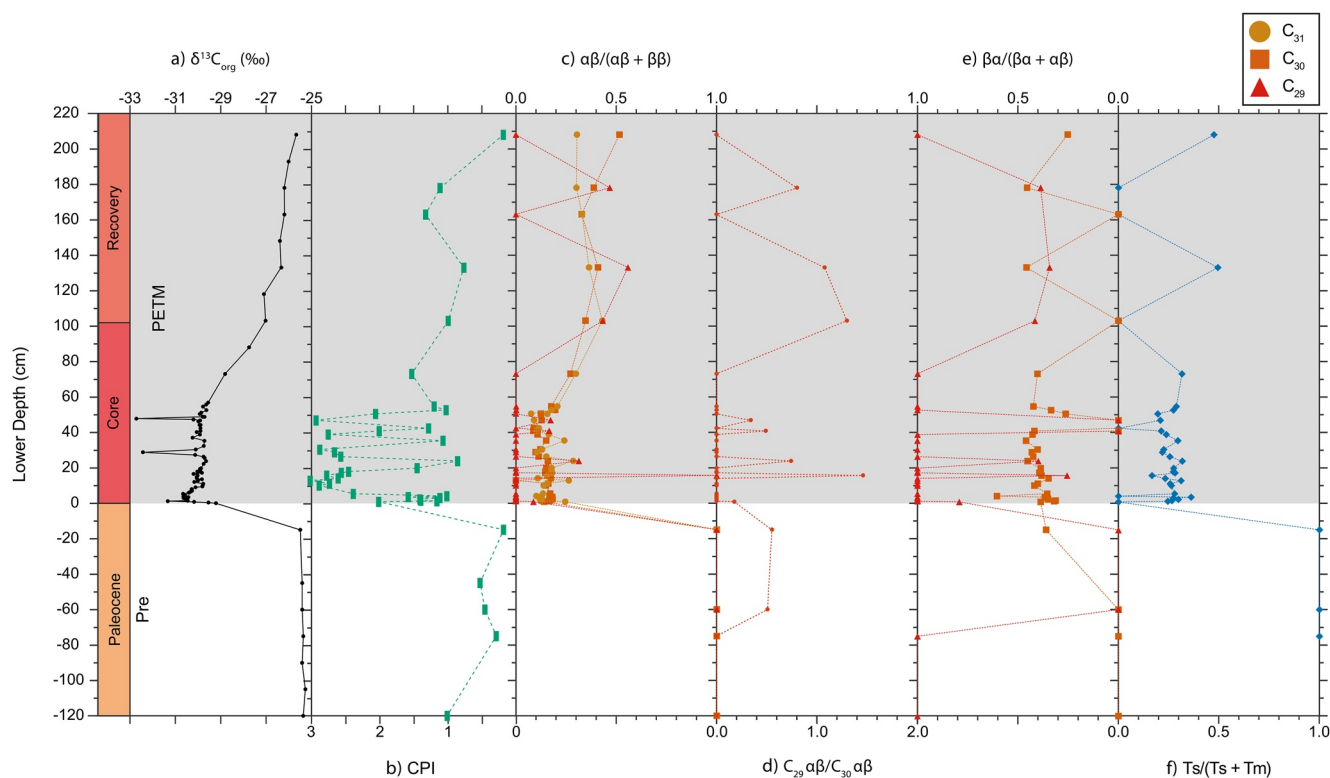


Figure 4. Thermal maturity ratios at Kheu River. Note some of the axis (CPI and $\beta\alpha/(\beta\alpha + \alpha\beta)$) are reversed to reflect increasing thermal maturity toward the right. (a) Bulk sediment $\delta^{13}\text{C}$ of organic carbon ($\delta^{13}\text{C}_{\text{org}}$) (Dickson et al., 2014), (b) CPI (this study), (c) $\alpha\beta/(\alpha\beta + \beta\beta)$ ratios (this study), (d) $\text{C}_{29}\alpha\beta/\text{C}_{30}\alpha\beta$ ratio (this study), (e) $\beta\alpha/(\beta\alpha + \alpha\beta)$ ratios (this study), and (f) $T_s/(T_s + T_m)$ ratio (this study). The PETM interval (including the core and recovery) is highlighted by gray shading.

3.1.5. TDP Site 14

$\text{C}_{16}\text{--}\text{C}_{33}$ *n*-alkanes and $\text{C}_{27}\text{--}\text{C}_{35}$ hopanes (including $\alpha\beta$, $\beta\alpha$, and $\beta\beta$ isomers) were identified in the apolar fraction. The CPI remains >3 (i.e., low thermal maturity), with the exception of five data points which occur during the core of the PETM (Figure 6b). Most noticeable is the large variability in the hopane-based thermal maturity ratios pre-PETM and for the first ~ 4 m of the core of the PETM. In the upper ~ 5 m of the core of the PETM, the ratios are more stable and in general agreement. This interval mostly exhibits more thermally mature values than during the pre-PETM section (e.g., $\text{C}_{31}\alpha\beta/(\alpha\beta + \beta\beta)$ increases by an average of 0.5; Figure 6c), suggesting a potential shift to an input of thermally mature organic carbon. For example, $\text{C}_{29\text{--}31}\alpha\beta/(\alpha\beta + \beta\beta)$ values are close to its mature endmember of 1 (Figure 6c).

3.2. OC_{petro} Mass Accumulation Rates

The OC_{petro} MARs were acquired from all the sites and grouped (where possible) into the key time intervals: (i) pre-PETM (Paleocene); (ii) the “core” (onset and body of the CIE) of the PETM; (iii) the recovery of the PETM; (iiia) Phase I of the recovery, and (iiib) Phase II of the recovery (see Text S1 in Supporting Information S1). To enable comparison between sites, we calculated the fold change in mean OC_{petro} MARs between pre-PETM and during the PETM (i.e., including the core and recovery of the PETM) (Figure 7). Overall, most of the sites display an increase in OC_{petro} MARs during the PETM (ACEX: $7 \times 10^{-2} \text{ gC cm}^{-2} \text{ Kyr}^{-1}$, Kheu River: $3 \times 10^{-2} \text{ gC cm}^{-2} \text{ Kyr}^{-1}$, Ancora: $2 \times 10^{-2} \text{ gC cm}^{-2} \text{ Kyr}^{-1}$, SDB: $6 \times 10^{-2} \text{ gC cm}^{-2} \text{ Kyr}^{-1}$, CamDor: $8 \times 10^{-3} \text{ gC cm}^{-2} \text{ Kyr}^{-1}$, TDP Site 14: and $8 \times 10^{-3} \text{ gC cm}^{-2} \text{ Kyr}^{-1}$). However, the sites with the largest increase are restricted to the mid-latitudes (i.e., Kheu River, Ancora, and SDB). In contrast, ODP Site 1172 exhibits a decrease ($3 \times 10^{-4} \text{ gC cm}^{-2} \text{ Kyr}^{-1}$) in OC_{petro} MAR during the PETM.

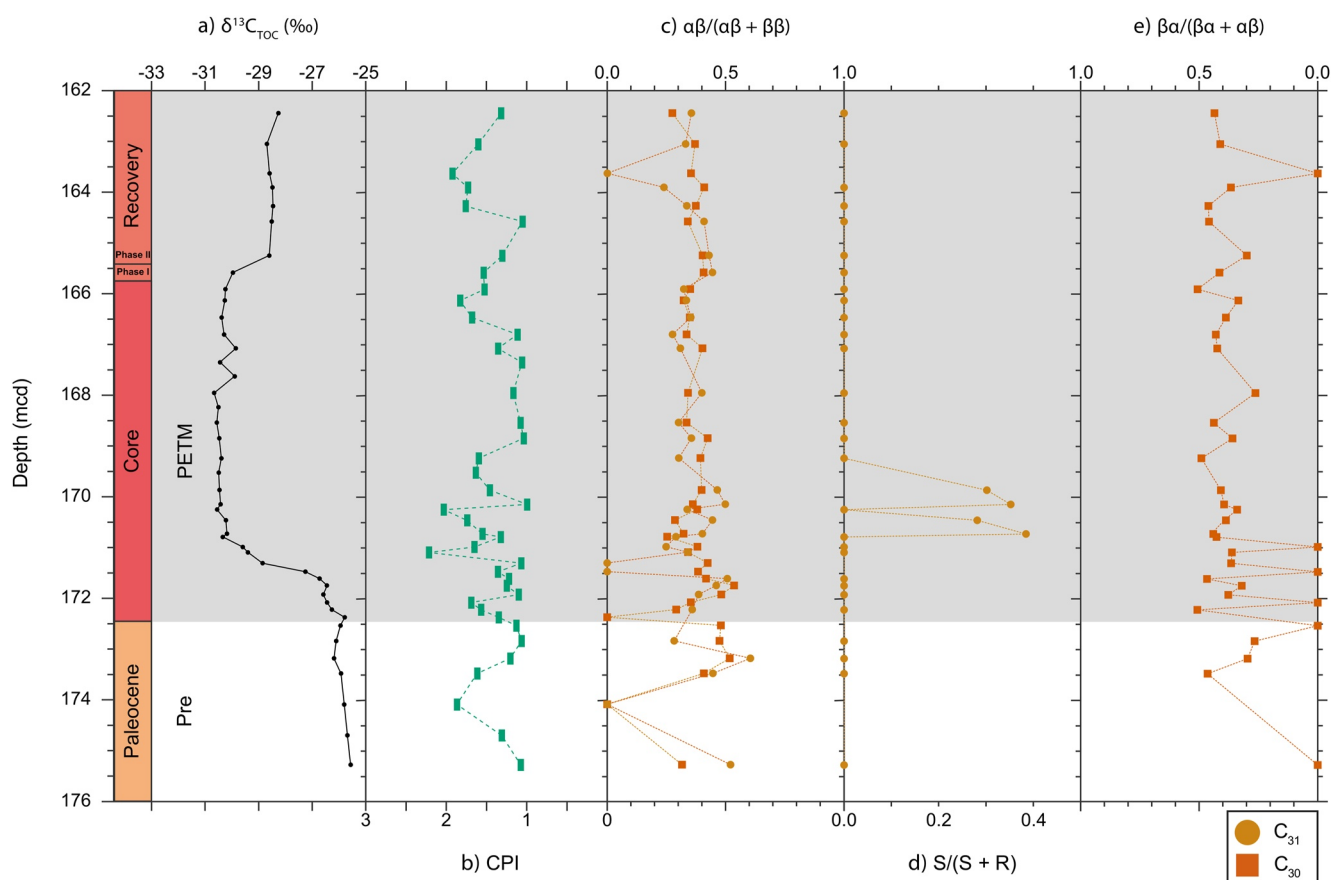


Figure 5. Thermal maturity ratios at Ancora. Note some of the axis (CPI and $\beta\alpha/(\beta\alpha + \alpha\beta)$) are reversed to reflect increasing thermal maturity toward the right. (a) bulk sediment $\delta^{13}\text{C}$ of total organic carbon ($\delta^{13}\text{C}_{\text{TOC}}$) (Elling et al., 2019), (b) CPI (this study), (c) $\alpha\beta/(\alpha\beta + \beta\beta)$ ratios (this study), (d) $S/(S + R)$ ratio (this study), and (e) $\beta\alpha/(\beta\alpha + \alpha\beta)$ ratio (this study). The PETM interval (including the core and recovery) is highlighted by gray shading.

4. Discussion

4.1. Enhanced OC_{petro} Mass Accumulation Rates in the Subtropics and Mid-Latitudes During the PETM

A previous study from Tanzania (TDP Site 14) reported a relative increase in the thermally mature $\alpha\beta$ hopanes during the PETM (Carmichael et al., 2017; Handley et al., 2012). Here, we present new hopane-based thermal maturity data that reveals rapidly fluctuating values within the first ~ 4 m of the core of the PETM (Figure 6). Similar patterns were observed in the bulk $\delta^{13}\text{C}$ of organic carbon ($\delta^{13}\text{C}_{\text{org}}$; Figure 6a), the n -alkane $\delta^{13}\text{C}$ record, the chain-length distributions of n -alkanes, and the branched and isoprenoid tetraether (BIT) index (Figure S2 in Supporting Information S1; Aze et al., 2014; Carmichael et al., 2017; Handley et al., 2008, 2012). The $\delta^{13}\text{C}_{\text{org}}$ and n -alkane $\delta^{13}\text{C}$ records were previously suggested to reflect episodic reworking of older (pre-PETM) material rather than changes in the atmospheric carbon reservoir (Aze et al., 2014; Handley et al., 2008). The hopane-based thermal maturity ratios within this study confirms this variable delivery of OC_{petro} . In contrast, the upper ~ 5 m of the core of the PETM exhibits more stability in the hopane-based thermal maturity ratios (Carmichael et al., 2017; Handley et al., 2012), $\delta^{13}\text{C}_{\text{org}}$ values, and n -alkane $\delta^{13}\text{C}$ values (Aze et al., 2014; Handley et al., 2008), indicating a switch from an episodic to persistent delivery of OC_{petro} (Carmichael et al., 2017; Handley et al., 2012). The hopane-based thermal maturity ratios also indicate that the OC_{petro} within this interval is of higher thermal maturity. During the PETM, a rise in thermally mature hopanes and LSRs increases OC_{petro} MARs by an average of $8 \times 10^{-3} \text{ gC cm}^{-2} \text{ Kyr}^{-1}$ (Figure 7). Enhanced OC_{petro} MAR is consistent with a shift from predominantly marine organic carbon to a terrestrial organic carbon source (e.g., an increase in the abundance of long-chain n -alkanes produced by vascular plants and brGDGTs produced by soil bacteria; Carmichael et al., 2017; Handley et al., 2008, 2012). Whilst there is greater LSR and terrigenous sediment during the PETM, C_{org} values declined. This drop was attributed to the larger contribution of clay (Handley et al., 2012). Evidence includes an abundance

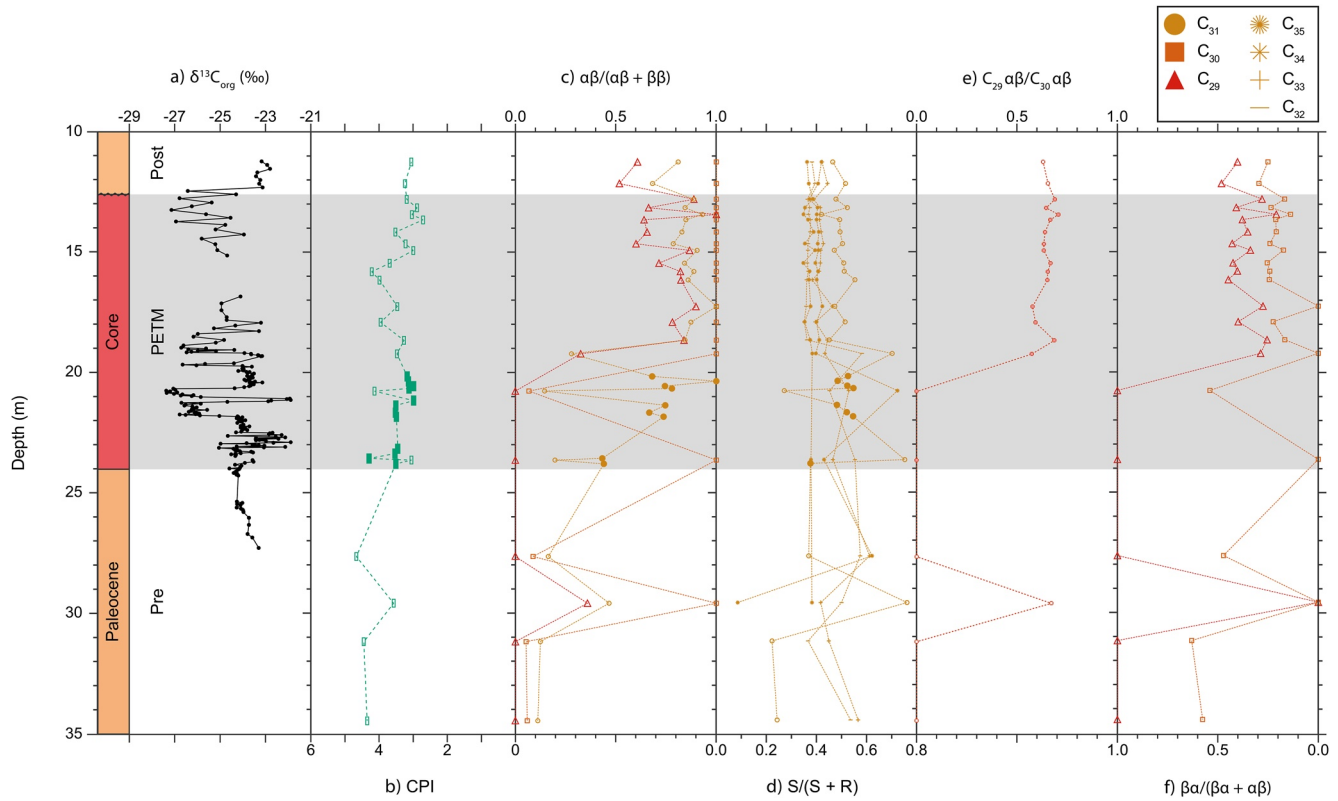


Figure 6. Thermal maturity ratios at TDP Site 14. Note some of the axis (CPI and $\beta\alpha/(\beta\alpha + \alpha\beta)$) are reversed to reflect increasing thermal maturity toward the right. (a) bulk sediment $\delta^{13}\text{C}_{\text{org}}$ of organic carbon ($\delta^{13}\text{C}_{\text{org}}$) (Aze et al., 2014), (b) CPI (closed symbols from this study and open symbols from Handley et al. (2012)), (c) $\alpha\beta/(\alpha\beta + \beta\beta)$ ratios (closed symbols from this study and open symbols from Handley et al. (2012)), (d) $S/(S + R)$ ratios (closed symbols from this study and open symbols from Handley et al., 2012), (e) $C_{29}\alpha\beta/C_{30}\alpha\beta$ ratio (Handley et al., 2012), and (f) $\beta\alpha/(\beta\alpha + \alpha\beta)$ ratios (Handley et al., 2012). The PETM interval (including the core) is highlighted by gray shading, and an unconformity truncates the CIE at 12.6 m.

of kaolinite, suggestive of intensified physical erosion (John et al., 2012), and high Li/Al combined with low Na/Al, suggestive of exhumation of older weathered clay. These additional proxies also indicate processes that support an increase in the mobilization and accumulation of OC_{petro} during the PETM.

Similar to Tanzania, Ancora exhibits an increase in the average OC_{petro} MARs (by $2 \times 10^{-2} \text{ gC cm}^{-2} \text{ Kyr}^{-1}$) during the PETM. This value falls within the average OC_{petro} MARs estimated at two other sites from the Atlantic Coastal Plain (i.e., SDB: $6 \times 10^{-2} \text{ gC cm}^{-2} \text{ Kyr}^{-1}$ and CamDor: $8 \times 10^{-3} \text{ gC cm}^{-2} \text{ Kyr}^{-1}$; Figure 7). However, the higher

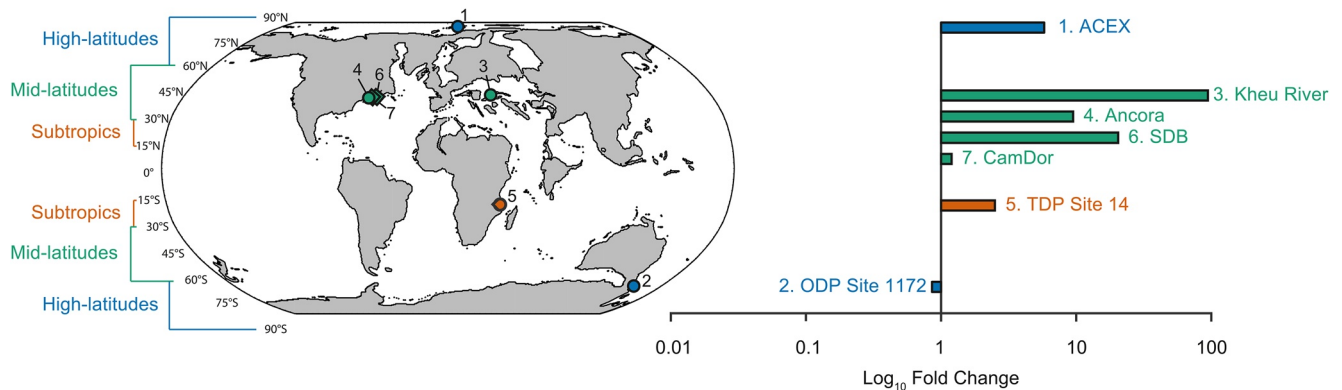


Figure 7. Log_{10} fold change in mean OC_{petro} mass accumulation rates (MARs) between pre-PETM and during the PETM (i.e., including the core and recovery of the PETM). The latitudes are defined as: high ($>60^\circ\text{N/S}$); mid- ($30\text{--}60^\circ\text{N/S}$); and subtropics ($15\text{--}30^\circ\text{N/S}$) (see Table S1 in Supporting Information S1).

OC_{petro} MAR is largely driven by a shift in LSR from 0.8 cm Kyr^{-1} (pre-PETM) to $11.28 \text{ cm Kyr}^{-1}$ (PETM) (Table 1; Stassen et al., 2012), and thus any uncertainty in the LSRs will also be reflected in the MAR estimates. The higher OC_{petro} MAR is consistent with evidence of terrestrial input to the Atlantic Coastal Plain during the PETM, including a higher abundance of kaolinite (Gibson et al., 2000), detrital magnetic minerals (Kopp et al., 2009), charcoal, seed pods, and terrestrial spores (Self-Trail et al., 2017). In addition, there is an increase in the terrestrial aquatic ratio (TAR; Bourbonniere & Meyers, 1996; Lyons et al., 2019). Indirect evidence includes changes in the marine microfossil assemblage toward benthic foraminifera (Self-Trail et al., 2017) and dinoflagellates (Sluijs & Brinkhuis, 2009) that can tolerate brackish water with high sediment input (Self-Trail et al., 2017). However, with the exception of the abrupt peaks of $C_{31} S/(S + R)$ at $\sim 169\text{--}171 \text{ mcd}$ (Figure 5d) and $C_{30} \beta\alpha/(\beta\alpha + \alpha\beta)$ at $\sim 171\text{--}173 \text{ mcd}$ (Figure 5e), the thermal maturity ratios at Ancora are relatively stable compared to SDB and CamDor (Lyons et al., 2019). Unlike Ancora, SDB and CamDor are characterized by a 6‰ increase in $\delta^{13}C_{\text{org}}$ values during the PETM (Lyons et al., 2019), which was argued to represent reworking of older (pre-PETM) material and not an increase in primary production (Lyons et al., 2019). This ^{13}C enrichment is not observed at Ancora (Figure 5a; Elling et al., 2019) and is consistent with the relatively stable thermal maturity ratios during the PETM.

The average OC_{petro} MARs at Kheu River exhibits an increase (by $3 \times 10^{-2} \text{ gC cm}^2 \text{ Kyr}^{-1}$) during the PETM (Figure 7), driven by an order-of-magnitude rise in C_{org} values from an average background level of $\sim 0.1 \text{ wt. \%}$ (pre- and post-PETM) to $\sim 4.4 \text{ wt. \%}$ (Dickson et al., 2014). However, in contrast to the sites discussed thus far, thermal maturity ratios at Kheu River shift to immature values during the core of the PETM (Figure 4). During the PETM, the *n*-alkane distribution is dominated by long-chain homologs characteristic of vascular plants (Dickson et al., 2014). It can therefore be argued that the shift observed in the thermal maturity ratios is mostly due to enhanced input of the OC_{bio} (i.e., immature hopanes such as $\beta\beta$ isomers) transported from land, although in situ production cannot be dismissed. An increase in the Chemical Index of Alteration (CIA) and spike in Ti/Al during the PETM not only corroborates evidence for terrestrial input but possibly erosion of older (pre-PETM) material (Dickson et al., 2014). As such, both OC_{petro} and (to a larger extent) OC_{bio} were likely delivered to this site. OC_{bio} burial may negate CO_2 released via enhanced OC_{petro} oxidation (e.g., Bowen & Zachos, 2010; John et al., 2008; Kaya et al., 2022; Papadomanolaki et al., 2022; Sluijs, Röhl, et al., 2008). Therefore, understanding whether the Kheu River region was a net carbon source or sink requires further investigations, and this study highlights the need to quantify both OC_{bio} and OC_{petro} in marine sediments. Regardless, the subtropical and mid-latitude sites all exhibit an increase in OC_{petro} MAR during the PETM, and thus suggest that OC_{petro} oxidation may provide an additional source of CO_2 .

4.2. Limited Change in Organic Carbon Sources in the High-Latitudes During the PETM

In the subtropics and mid-latitudes, average OC_{petro} MAR increased between 8×10^{-3} and $6 \times 10^{-2} \text{ gC cm}^2 \text{ Kyr}^{-1}$ during the PETM for a given site (see Section 4.1). In the high-latitudes, OC_{petro} MARs in the Arctic (ACEX) and the southwest Pacific Ocean (ODP Site 1172) either increase (by $7 \times 10^{-2} \text{ gC cm}^2 \text{ Kyr}^{-1}$) or decrease (by $3 \times 10^{-4} \text{ gC cm}^2 \text{ Kyr}^{-1}$), respectively (Figure 7). The decline observed at ODP Site 1172 is due to a small drop in C_{org} values and LSRs. The marked rise at ACEX is mostly driven by a peak in TOC values, from a minimum of 1.3% (pre-PETM) to a maximum of 4.9% (core PETM) (Elling et al., 2019). Absolute abundances of paly-nomorphs from ACEX suggest that TOC is a mixture of marine and terrestrial organic matter (Sluijs, Röhl, et al., 2008). However, both sites, with the exception of the $C_{31} S/(S + R)$ ratio at ODP Site 1172 (Figure 3d), have stable thermal maturity ratios throughout the record. This indicates that although the supply of organic carbon increased during the PETM, the organic carbon source did not distinctly change. Intriguingly, there is an antiphase relationship between $C_{30} \alpha\beta/(\alpha\beta + \beta\beta)$ and $C_{31} \alpha\beta/(\alpha\beta + \beta\beta)$ at ACEX (Figure 2c), perhaps suggesting subtle changes in the organic carbon source during the PETM. Decoupling between the C_{30} and C_{31} indices could be due to a greater input of acidic peats, which are dominated by $C_{31} \alpha\beta$ hopanes but lack abundant $C_{30} \alpha\beta$ isomers (Inglis et al., 2018). The contribution of OC_{bio} from acidic peats at ACEX has also been inferred from brGDGTs (Sluijs et al., 2020).

4.3. Climate Exerts Primary Control on OC_{petro} Mobilization During the PETM

Various factors may explain why some shallow marine sediments are characterized by enhanced delivery of OC_{petro} during the PETM. Modern observations have identified a strong link between rainfall and efficient

erosion/transfer of organic carbon from land-to-sea (e.g., T. I. Eglinton et al., 2021; Hilton, 2017). In the subtropics, evidence for changes in the hydrological cycle during the PETM are scarce. Previous work at TDP Site 14 revealed that the hydrogen isotope of *n*-alkanes ($\delta^2\text{H}_{n\text{-alkanes}}$) increased during the PETM, which was inferred to represent a shift toward more arid climate conditions (Carmichael et al., 2017; Handley et al., 2008). Enhanced aridity could lead to minimal vegetation cover, hindering soil development, and maximizing the potential for erosion and mobilization of OC_{petro} (e.g., Hilton et al., 2008; Leithold et al., 2006). Furthermore, there are large fluctuations in $\delta^2\text{H}_{n\text{-alkanes}}$ values, which may indicate oscillations between dry and wet climate states and/or an increase in extreme precipitation events (Carmichael et al., 2017; Handley et al., 2008). Modeling studies over subtropical Africa during the PETM support the latter (Carmichael et al., 2018). Episodic and intense rainfall on a landscape prone to erosion would explain the highly variable delivery of different organic carbon sources, as shown by the hopane-based thermal maturity data (this study), $\delta^{13}\text{C}_{\text{org}}$ values, and *n*-alkane $\delta^{13}\text{C}$ values (Aze et al., 2014; Handley et al., 2008).

Analogous to TDP Site 14, Kheu River also exhibits high variability in the thermal maturity ratios (e.g., CPI, $\text{C}_{29} \alpha\beta/\text{C}_{30} \alpha\beta$, and $\text{C}_{29} \beta\alpha/(\beta\alpha + \alpha\beta)$; Figure 4), chain-length distributions of *n*-alkanes, BIT index, grain-size, and CIA during the PETM (Dickson et al., 2014). Although two brief intervals of marine transgression have been noted in this region (Shcherbinina et al., 2016), the biomarker records are more variable and thus appear to be more consistent with episodic changes in precipitation. There are multiple lines of evidences associating other mid-latitude sites with increased transient and extreme rainfall events during the PETM. For example, the deposition of conglomerates in the Pyrenees (Chen et al., 2018; Schmitz & Pujalte, 2003, 2007), changes in paleosol weathering indices, and the abundance and composition of nodules in the Bighorn Basin (e.g., Kraus & Riggins, 2007; Kraus et al., 2013). There is also evidence for greater freshwater runoff in the Atlantic Coastal Plain (i.e., Ancora, SDB, and CamDor) during the PETM, with the development of a river-dominated shelf referred to as the “Appalachian Amazon” (Doubrawa et al., 2022; Kopp et al., 2009; Self-Trail et al., 2017). This is consistent with high-resolution climate models that suggest the western Atlantic region was dominated by an increase in extratropical cyclones and more extreme rainfall events (Kiehl et al., 2021; Rush et al., 2021; Shields et al., 2021). Although the hydrological cycle likely exerted a first-order control on the mobilization of terrestrial organic carbon, other ecological and/or geologic controls could have also been important. For example, the dominance of OC_{bio} at Kheu River may reflect abundant vegetation cover (e.g., Goñi et al., 2013). On the other hand, the dominance of OC_{petro} at TDP Site 14 may reflect greater availability of OC_{petro} -rich rock and/or exacerbated erosion of OC_{petro} caused by limited soil and vegetation (e.g., Hilton et al., 2011).

Model simulations indicate an increase in precipitation in the high-latitudes for a PETM-type warming event (e.g., Carmichael et al., 2016; Cramwinckel et al., 2023; Winguth et al., 2010). Proxies also reconstruct northern and southern high-latitudes to be wetter at the onset of the PETM (e.g., evidence from palynomorphs (Korasidis et al., 2022; Sluijs et al., 2006; Willard et al., 2019), fossilized plants (Harding et al., 2011), the hydrogen isotopic composition of *n*-alkanes ($\delta^2\text{H}_{n\text{-alkanes}}$; Pagani et al., 2006), and clay-mineralogy (Dypvik et al., 2011; Kaiho et al., 1996; Robert & Kennett, 1994)). Yet, biomarker evidence from high-latitude sites (i.e., ACEX and ODP Site 1172) indicates limited changes in the source of organic carbon during the PETM. This suggests that in order to exhume and mobilize OC_{petro} , changes in rainfall seasonality and frequency of extreme precipitation events may be required (see Section 4.1). Alternatively, there may be other feedback mechanisms and/or more regional controls beyond the hydrological cycle. In modern systems, local geomorphic processes play a strong role in regulating OC_{petro} transport from land-to-sea (e.g., Hilton & West, 2020). Variability in OC_{petro} MARs could also be attributed to changes in sea level during the PETM. Indeed, various studies have suggested marine transgression during the PETM, including: ACEX (Sluijs et al., 2006); ODP Site 1172 (Sluijs et al., 2011); Kheu River (Shcherbinina et al., 2016); the Atlantic Coastal Plain (John et al., 2008); and elsewhere (Jiang et al., 2023; Li et al., 2020 and references therein; Sluijs, Brinkhuis, et al., 2008 and references therein). However, although sea level rise is expected to reduce the supply of terrestrial organic carbon into the marine realm, this is rarely observed (e.g., Sluijs et al., 2014) and most PETM sites are characterized by enhanced terrigenous material during the PETM (Carmichael et al., 2017 and references therein).

4.4. Timing and Implications for CO_2 Release During the PETM

Enhanced OC_{petro} delivery was suggested to have occurred ~10–20 Kyr after the onset of the PETM (i.e., within the body of the CIE) by Lyons et al. (2019). Here, we confirm that elevated OC_{petro} MARs occurred within the

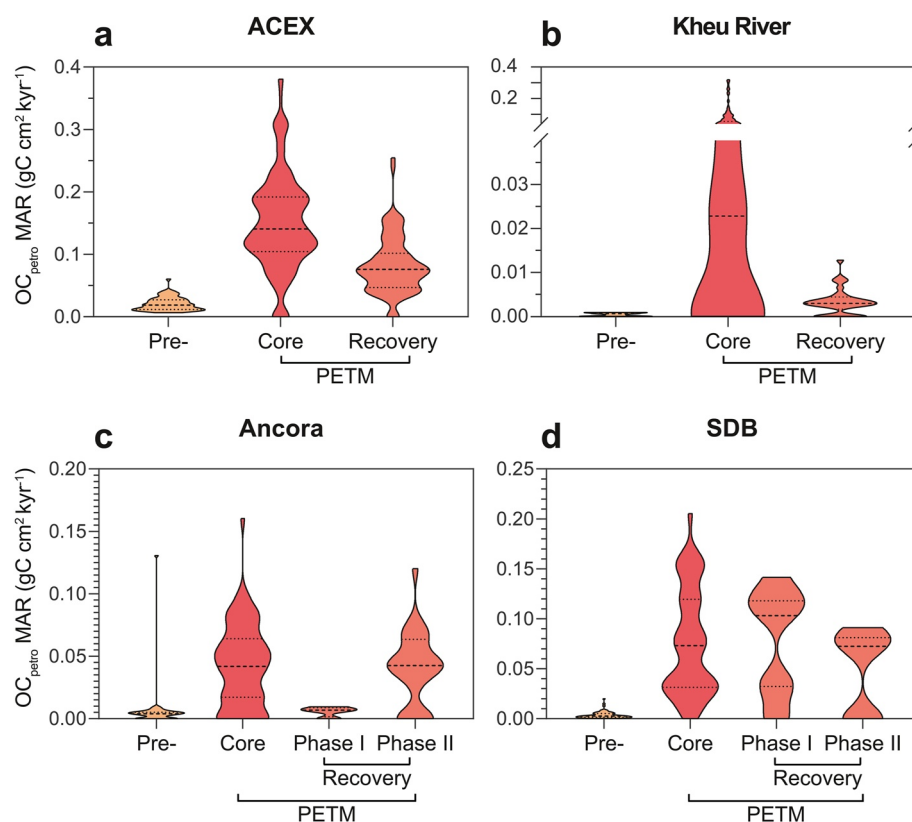


Figure 8. Violin plots of OC_{petro} MARs ($gC\ cm^{-2}\ Kyr^{-1}$) for the defined time intervals of sites with the recovery phase (a) ACEX, (b) Kheu River, (c) Ancora, and (d) SDB. The thick dashed line represents the median and the thin dashed line extends from the 25th to 75th percentiles. Note the discontinuous y-axis and two different scales of (b) Kheu River.

core of the PETM at several other sites (i.e., ACEX, Kheu River, Ancora; Figure 8). However, the exact timing within the core (i.e., onset or body) cannot be determined due to the lack of robust age constraints. The sites where the recovery phases were defined (i.e., ACEX, Kheu River, Ancora, and SDB), enables insight into whether enhanced OC_{petro} MARs continued after the core interval or recovered to pre-PETM values. Interestingly, at both Ancora and SDB, median OC_{petro} MARs are higher than the core of the PETM in Phase II and I, respectively (Figure 8). There is a decrease in OC_{petro} MAR during Phase I of the recovery at Ancora, however this interval consists of a single data point. Although an increase in OC_{petro} MAR during the recovery is not observed at ACEX and Kheu River, values do not return to pre-PETM levels. This suggests that at certain localities, terrestrial organic carbon cycle perturbations continued into the recovery phase. If OC_{petro} was oxidized, it may have provided an additional source of CO_2 during the recovery. In this scenario, other negative feedback mechanisms are required to negate the additional carbon released and help assist in the recovery of the PETM. Several processes have been proposed, such as silicate weathering (Penman et al., 2014) and/or enhanced OC_{bio} burial, either on land (Bowen, 2013; Bowen & Zachos, 2010) or within the ocean (John et al., 2008; Ma et al., 2014). For example, exacerbated weathering and erosion during the PETM (Pogge von Strandmann et al., 2021) may increase nutrient delivery from land-to-sea, stimulating primary productivity and therefore OC_{bio} burial (Kaya et al., 2022; Papadomanolaki et al., 2022). However, the source of sequestered organic carbon in ocean sediments (i.e., terrestrial vs. marine) remains a major source of uncertainty.

Overall, Lyons et al. (2019) inferred between 10^2 and 10^4 PgC was released as CO_2 globally due to oxidation of OC_{petro} during the PETM. This assumed that the three sites (i.e., SDB, CamDor, and TDP Site 14) are globally representative. However, this study demonstrates that enhanced OC_{petro} MARs was mostly restricted to the subtropics and mid-latitudes, suggesting that global estimates may be lower than previously inferred. In addition, the maximum value of 10^4 PgC assumed that 85% of OC_{petro} was oxidized. However, increased erosion of clastic sediments can aid the preservation of OC_{petro} (e.g., Bouchez et al., 2014; Burdige, 2007). Furthermore, intense precipitation events (characteristic of the subtropics and mid-latitudes; e.g., Carmichael et al., 2017;

Handley et al., 2008; Kiehl et al., 2021; Kraus & Riggins, 2007; Kraus et al., 2013; Rush et al., 2021; Schmitz & Pujalte, 2003, 2007; Shields et al., 2021) may reduce the transfer time of OC_{petro} from source to sink, thereby reducing the possibility for oxidation (e.g., Hilton et al., 2011). However, it is important to consider that shallow marine sites will likely integrate an expansive catchment area, which incorporate slow meandering rivers as well as steep mountainous rivers. In the former system, the extent of OC_{petro} oxidized could be as high as ~90% (e.g., Bouchez et al., 2010; Galy et al., 2008). This is especially likely at sites where large freshwater input was evident, such as the Atlantic Coastal Plain (Doubrawa et al., 2022; Kopp et al., 2009; Self-Trail et al., 2017). We also demonstrate that CO_2 release may have continued into the recovery of the PETM, suggesting that other feedback mechanisms (e.g., OC_{bio} burial) were necessary to aid in the recovery of the Earth's climate system. To constrain global estimates of CO_2 emitted from OC_{petro} oxidation, future work is required to elucidate these uncertainties. For example, Raman spectroscopy could help identify the oxidation efficiency based on the degree of highly degradable versus recalcitrant organic carbon (Sparkes et al., 2018), whilst paleo-digital elevation models may provide further insight on sediment routing systems and transit time during the PETM (Lyster et al., 2020).

5. Conclusion

This study uses a multi-biomarker approach to reconstruct the mobilization of petrogenic organic carbon (OC_{petro}) during the PETM. We find widespread evidence for enhanced OC_{petro} mass accumulation rates (MARs) in the subtropics and mid-latitudes during the PETM. In this region, we argue that extreme rainfall events exacerbated erosion, mobilization, and burial of OC_{petro} in the marine realm. In addition, we demonstrate that high OC_{petro} MARs persisted into the recovery phase of the PETM. However, the high-latitude sites do not exhibit a distinct change in the source of organic carbon during the PETM. This may be due to a more stable hydrological regime and/or additional controls, such as geomorphic processes or sea level change. Overall, OC_{petro} oxidation likely acted as an additional source of CO_2 during the PETM. However, further work is needed to determine the exact contributions of OC_{petro} as a positive feedback mechanism during the PETM and other transient warming events.

Conflict of Interest

The authors declare no conflicts of interest relevant to this study.

Data Availability Statement

The processed data used in this study are available at OSF and associated with a CC-BY Attribution 4.0 International license (Hollingsworth, 2023).

References

- Aze, T., Pearson, P. N., Dickson, A. J., Badger, M. P. S., Bown, P. R., Pancost, R. D., et al. (2014). Extreme warming of tropical waters during the Paleocene—Eocene Thermal Maximum. *Geology*, 42(9), 739–742. <https://doi.org/10.1130/G35637.1>
- Berhe, A. A., Harte, J., Harden, J. W., & Torn, M. S. (2007). The significance of the erosion-induced terrestrial carbon sink. *BioScience*, 57(4), 337–346. <https://doi.org/10.1641/B570408>
- Berner, R. A., & Caldeira, K. (1997). The need for mass balance and feedback in the geochemical carbon. *Geology*, 25(10), 955–956. [https://doi.org/10.1130/0091-7613\(1997\)025<0955](https://doi.org/10.1130/0091-7613(1997)025<0955)
- Berner, R. A., Lasaga, A. C., & Garrels, R. M. (1983). The carbonate-silicate geochemical cycle and its effect on atmospheric carbon dioxide over the past 100 million years. *American Journal of Science*, 283(7), 641–683. <https://doi.org/10.2475/ajs.283.7.641>
- Bianchi, T. S., Cui, X., Blair, N. E., Burdige, D. J., Eglinton, T. I., & Galy, V. (2018). Centers of organic carbon burial and oxidation at the land-ocean interface. *Organic Geochemistry*, 115, 138–155. <https://doi.org/10.1016/j.orggeochem.2017.09.008>
- Blair, N. E., Leithold, E. L., Ford, S. T., Peeler, K. A., Holmes, J. C., & Perkey, D. W. (2003). The persistence of memory: The fate of ancient sedimentary organic carbon in a modern sedimentary system. *Geochimica et Cosmochimica Acta*, 67(1), 63–73. [https://doi.org/10.1016/S0016-7037\(02\)01043-8](https://doi.org/10.1016/S0016-7037(02)01043-8)
- Bolle, M. P., Pardo, A., Hinrichs, K. U., Adatte, T., Von Salis, K., Burns, S., et al. (2000). The Paleocene-Eocene transition in the marginal north-eastern Tethys (Kazakhstan and Uzbekistan). *International Journal of Earth Sciences*, 89(2), 390–414. <https://doi.org/10.1007/s005310000092>
- Bouchez, J., Beyssac, O., Galy, V., Gaillardet, J., France-lanord, C., Maurice, L., & Moreira-turcq, P. (2010). Oxidation of petrogenic organic carbon in the Amazon floodplain as a source of atmospheric CO_2 . *Geology*, 38(3), 255–258. <https://doi.org/10.1130/G30608.1>
- Bouchez, J., Galy, V., Hilton, R. G., Gaillardet, J. Ô., Moreira-Turcq, P., Pérez, M. A., et al. (2014). Source, transport and fluxes of Amazon River particulate organic carbon: Insights from river sediment depth-profiles. *Geochimica et Cosmochimica Acta*, 133, 280–298. <https://doi.org/10.1016/j.gca.2014.02.032>
- Bourbonniere, R. A., & Meyers, P. A. (1996). Sedimentary geolipid records of historical changes in the watersheds and productivities of Lakes Ontario and Erie. *Limnology & Oceanography*, 41(2), 352–359. <https://doi.org/10.4319/lo.1996.41.2.0352>

Acknowledgments

G.N. Inglis is supported by a GCRF Royal Society Dorothy Hodgkin Fellowship (DHF/R1/191178) with additional support via the Royal Society (RF\ERE/231019, RF\ERE/210068). E.H. Hollingsworth acknowledges funding from a NERC (Grant NE/S007210). This research used samples provided by the Ocean Drilling Program (ODP) and the International Ocean Drilling Program (IODP). F.J. Elling is supported by Deutsche Forschungsgemeinschaft Grant (441217575) and A. Pearson was supported by the US National Science Foundation (Grant OCE-1843285). We thank Sargent Bray at the University of Southampton and Katiana Doeana and Susan Carter at Harvard University for laboratory assistance. For TDP Site 14 samples, we thank colleagues in the Tanzanian Drilling Project, and especially those from the Tanzanian Petroleum Development Corporation. Partial funding for M.P.S. Badger was provided by NERC Grant (NE/H006273/1). For Kheu River samples, we thank E.A. Shcherbinina, Y. Gavrilov, and A.J. Dickson who is supported by UKRI Frontier Research Grant (EP/X022080/1). We thank the NERC Life Sciences Mass Spectrometry Facility for technical support of the GC-MS and NERC for partial funding of the mass spectrometry facilities at Bristol (R8/H10/63). N.M. Papadomanolaki acknowledges funding from The Netherlands Earth System Science Center (NESSC), financially supported by the Ministry of Education, Culture and Science (OCW). We thank Arnold van Dijk for analytical assistance.

- Bowen, G. J. (2013). Up in smoke: A role for organic carbon feedbacks in Paleogene hyperthermals. *Global and Planetary Change*, *109*, 18–29. <https://doi.org/10.1016/j.gloplacha.2013.07.001>
- Bowen, G. J., Bralower, T. J., Delaney, M. L., Dickens, G. R., Kelly, D. C., Koch, P. L., et al. (2006). Eocene hyperthermal event offers insight into greenhouse warming. *Eos*, *87*(17), 165–169. <https://doi.org/10.1029/2006eo170002>
- Bowen, G. J., & Zachos, J. C. (2010). Rapid carbon sequestration at the termination of the Paleocene-Eocene Thermal Maximum. *Nature Geoscience*, *3*(12), 866–869. <https://doi.org/10.1038/ngeo1014>
- Bray, E. E., & Evans, E. D. (1961). Distribution of n-paraffins as a clue to recognition of source beds. *Geochimica et Cosmochimica Acta*, *22*(1), 2–15. [https://doi.org/10.1016/0016-7037\(61\)90069-2](https://doi.org/10.1016/0016-7037(61)90069-2)
- Burdige, D. J. (2007). Preservation of organic matter in marine sediments: Controls, mechanisms, and an imbalance in sediment organic carbon budgets? *Chemical Reviews*, *107*(2), 467–485. <https://doi.org/10.1021/cr050347q>
- Bush, R. T., & McInerney, F. A. (2013). Leaf wax n-alkane distributions in and across modern plants: Implications for paleoecology and chemotaxonomy. *Geochimica et Cosmochimica Acta*, *117*, 161–179. <https://doi.org/10.1016/j.gca.2013.04.016>
- Carmichael, M. J., Inglis, G. N., Badger, M. P. S., Naafs, B. D. A., Behrooz, L., Rimmelzwaal, S., et al. (2017). Hydrological and associated biogeochemical consequences of rapid global warming during the Paleocene-Eocene Thermal Maximum. *Global and Planetary Change*, *157*, 114–138. <https://doi.org/10.1016/j.gloplacha.2017.07.014>
- Carmichael, M. J., Lunt, D. J., Huber, M., Heinemann, M., Kiehl, J., LeGrande, A., et al. (2016). A model-model and data-model comparison for the early Eocene hydrological cycle. *Climate of the Past*, *12*(2), 455–481. <https://doi.org/10.5194/cp-12-455-2016>
- Carmichael, M. J., Pancost, R. D., & Lunt, D. J. (2018). Changes in the occurrence of extreme precipitation events at the Paleocene–Eocene Thermal Maximum. *Earth and Planetary Science Letters*, *501*, 24–36. <https://doi.org/10.1016/j.epsl.2018.08.005>
- Chen, C., Guerit, L., Foreman, B. Z., Hassenruck-Gudipati, H. J., Adatte, T., Honegger, L., et al. (2018). Estimating regional flood discharge during Paleocene-Eocene global warming. *Scientific Reports*, *8*(1), 1–8. <https://doi.org/10.1038/s41598-018-31076-3>
- Clark, K. E., Hilton, R. G., West, A. J., Robles Caceres, A., Gröcke, D. R., Marthews, T. R., et al. (2017). Erosion of organic carbon from the Andes and its effects on ecosystem carbon dioxide balance. *Journal of Geophysical Research: Biogeosciences*, *122*(3), 449–469. <https://doi.org/10.1002/2016JG003615>
- Clark, K. E., Stallard, R. F., Murphy, S. F., Scholl, M. A., González, G., Plante, A. F., & McDowell, W. H. (2022). Extreme rainstorms drive exceptional organic carbon export from forested humid-tropical rivers in Puerto Rico. *Nature Communications*, *13*(1), 1–8. <https://doi.org/10.1038/s41467-022-29618-5>
- Cramwinckel, M. J., Burls, N. J., Fahad, A. A., Knapp, S., West, C. K., Reichgelt, T., et al. (2023). Global and zonal-mean hydrological response to early Eocene warmth. *Paleoceanography and Paleoclimatology*, *38*(6), 1–21. <https://doi.org/10.1029/2022PA004542>
- Cui, Y., Diefendorf, A. F., Kump, L. R., Jiang, S., & Freeman, K. H. (2021). Synchronous marine and terrestrial carbon cycle perturbation in the high Arctic during the PETM. *Paleoceanography and Paleoclimatology*, *36*(4), 1–21. <https://doi.org/10.1029/2020PA003942>
- Deconto, R. M., Galeotti, S., Pagani, M., Tracy, D., Schaefer, K., Zhang, T., et al. (2012). Past extreme warming events linked to massive carbon release from thawing permafrost. *Nature*, *484*(7392), 87–91. <https://doi.org/10.1038/nature10929>
- Dickens, G. R. (2011). Down the Rabbit Hole: Toward appropriate discussion of methane release from gas hydrate systems during the Paleocene-Eocene Thermal Maximum and other past hyperthermal events. *Climate of the Past*, *7*(3), 831–846. <https://doi.org/10.5194/cp-7-831-2011>
- Dickens, G. R., Castillo, M. M., & Walker, J. C. G. (1997). A blast of gas in the latest Paleocene: Simulating first-order effects of massive dissociation of oceanic methane hydrate. *Geology*, *25*(3), 259–262. [https://doi.org/10.1130/0091-7613\(1997\)025<0259:ABOGIT>2.3.CO;2](https://doi.org/10.1130/0091-7613(1997)025<0259:ABOGIT>2.3.CO;2)
- Dickens, G. R., O’Neil, J. R., Rea, D. K., & Owen, R. M. (1995). Dissociation of oceanic methane hydrate as a cause of the carbon isotope excursion at the end of the Paleocene. *Paleoceanography*, *10*(6), 965–971. <https://doi.org/10.1029/95PA02087>
- Dickson, A. J., Rees-owen, R. L., März, C., Coe, A. L., Cohen, A. S., Pancost, R. D., et al. (2014). The spread of marine anoxia on the northern Tethys margin during the Paleocene-Eocene Thermal Maximum. *Paleoceanography*, *29*(6), 471–488. <https://doi.org/10.1002/2014PA002629>
- Received
- Diefendorf, A. F., & Freimuth, E. J. (2017). Extracting the most from terrestrial plant-derived n-alkyl lipids and their carbon isotopes from the sedimentary record: A review. *Organic Geochemistry*, *103*, 1–21. <https://doi.org/10.1016/j.orggeochem.2016.10.016>
- Doubrawa, M., Stassen, P., Robinson, M. M., Babila, T. L., Zachos, J. C., & Speijer, R. P. (2022). Shelf ecosystems along the U.S. Atlantic Coastal Plain prior to and during the Paleocene-Eocene Thermal Maximum: Insights into the stratigraphic architecture. *Paleoceanography and Paleoclimatology*, *37*(10), 1–21. <https://doi.org/10.1029/2022PA004475>
- Dunkley Jones, T., Manners, H. R., Hoggett, M., Kirtland Turner, S., Westerhold, T., Leng, M. J., et al. (2018). Dynamics of sediment flux to a bathyal continental margin section through the Paleocene–Eocene Thermal Maximum. *Climate of the Past*, *14*(7), 1035–1049. <https://doi.org/10.5194/cp-14-1035-2018>
- Dypvik, H., Riber, L., Burca, F., Rütger, D., Jørgvoll, D., Nagy, J., & Jochmann, M. (2011). The Paleocene-Eocene Thermal Maximum (PETM) in Svalbard—Clay mineral and geochemical signals. *Palaeogeography, Palaeoclimatology, Palaeoecology*, *302*(3–4), 156–169. <https://doi.org/10.1016/j.palaeo.2010.12.025>
- Eglinton, G., & Hamilton, R. J. (1967). Leaf epicuticular waxes. *Science*, *156*(3780), 1322–1335. <https://doi.org/10.1126/science.156.3780.1322>
- Eglinton, T. I., Galy, V. V., Hemingway, J. D., Feng, X., Bao, H., Blattmann, T. M., et al. (2021). Climate control on terrestrial biospheric carbon turnover. *Proceedings of the National Academy of Sciences of the United States of America*, *118*(8). <https://doi.org/10.1073/pnas.2011585118>
- Elling, F. J., Gottschalk, J., Doeana, K. D., Kusch, S., Hurley, S. J., & Pearson, A. (2019). Archaeal lipid biomarker constraints on the Paleocene-Eocene carbon isotope excursion. *Nature Communications*, *10*(1), 1–10. <https://doi.org/10.1038/s41467-019-12553-3>
- Farrimond, P., Taylor, A., & Telnás, N. (1998). Biomarker maturity parameters: The role of generation and thermal degradation. *Organic Geochemistry*, *29*(5–7), 1181–1197. [https://doi.org/10.1016/S0146-6380\(98\)00079-5](https://doi.org/10.1016/S0146-6380(98)00079-5)
- French, K. L., Tosca, N. J., Cao, C., & Summons, R. E. (2012). Diagenetic and detrital origin of moretane anomalies through the Permian-Triassic boundary. *Geochimica et Cosmochimica Acta*, *84*, 104–125. <https://doi.org/10.1016/j.gca.2012.01.004>
- Frieling, J., Svensen, H. H., Planke, S., Cramwinckel, M. J., Selnes, H., & Sluijs, A. (2016). Thermogenic methane release as a cause for the long duration of the PETM. *Proceedings of the National Academy of Sciences of the United States of America*, *113*(43), 12059–12064. <https://doi.org/10.1073/pnas.1603348113>
- Galy, V., Beyssac, O., France-Lanord, C., & Eglinton, T. (2008). Recycling of graphite during Himalayan erosion: A geological stabilization of carbon in the crust. *Science*, *322*(5903), 943–945. <https://doi.org/10.1126/science.1161408>
- Galy, V., France-Lanord, C., Beyssac, O., Faure, P., Kudrass, H., & Palhol, F. (2007). Efficient organic carbon burial in the Bengal fan sustained by the Himalayan erosional system. *Nature*, *450*(7168), 407–410. <https://doi.org/10.1038/nature06273>
- Galy, V., Peucker-Ehrenbrink, B., & Eglinton, T. (2015). Global carbon export from the terrestrial biosphere controlled by erosion. *Nature*, *521*(7551), 204–207. <https://doi.org/10.1038/nature14400>

- Gibson, T. G., Bybell, L. M., & Mason, D. B. (2000). Stratigraphic and climatic implications of clay mineral changes around the Paleocene/Eocene boundary of the northeastern US margin. *Sedimentary Geology*, 134(1–2), 65–92. [https://doi.org/10.1016/S0037-0738\(00\)00014-2](https://doi.org/10.1016/S0037-0738(00)00014-2)
- Gofñi, M. A., Hatten, J. A., Wheatcroft, R. A., & Borgeld, J. C. (2013). Particulate organic matter export by two contrasting small mountainous rivers from the Pacific Northwest, U.S.A. *Journal of Geophysical Research: Biogeosciences*, 118(1), 112–134. <https://doi.org/10.1002/jgrg.20024>
- Gutjahr, M., Ridgwell, A., Sexton, P. F., Anagnostou, E., Pearson, P. N., Pälike, H., et al. (2017). Very large release of mostly volcanic carbon during the Palaeocene–Eocene Thermal Maximum. *Nature*, 548(7669), 573–577. <https://doi.org/10.1038/nature23646>
- Handley, L., Crouch, E. M., & Pancost, R. D. (2011). A New Zealand record of sea level rise and environmental change during the Paleocene-Eocene Thermal Maximum. *Palaeogeography, Palaeoclimatology, Palaeoecology*, 305(1–4), 185–200. <https://doi.org/10.1016/j.palaeo.2011.03.001>
- Handley, L., O'Halloran, A., Pearson, P. N., Hawkins, E., Nicholas, C. J., Schouten, S., et al. (2012). Changes in the hydrological cycle in tropical East Africa during the Paleocene-Eocene Thermal Maximum. *Palaeogeography, Palaeoclimatology, Palaeoecology*, 329–330, 10–21. <https://doi.org/10.1016/j.palaeo.2012.02.002>
- Handley, L., Pearson, P. N., Mcmillan, I. K., & Pancost, R. D. (2008). Large terrestrial and marine carbon and hydrogen isotope excursions in a new Paleocene/Eocene boundary section from Tanzania. *Earth and Planetary Science Letters*, 275(1), 17–25. <https://doi.org/10.1016/j.epsl.2008.07.030>
- Harding, I. C., Charles, A. J., Marshall, J. E. A., Pälike, H., Roberts, A. P., Wilson, P. A., et al. (2011). Sea-level and salinity fluctuations during the Paleocene-Eocene thermal maximum in Arctic Spitsbergen. *Earth and Planetary Science Letters*, 303(1–2), 97–107. <https://doi.org/10.1016/j.epsl.2010.12.043>
- Hilton, R. G. (2017). Climate regulates the erosional carbon export from the terrestrial biosphere. *Geomorphology*, 277, 118–132. <https://doi.org/10.1016/j.geomorph.2016.03.028>
- Hilton, R. G., Gaillardet, J., Calmels, D., & Birck, J. (2014). Geological respiration of a mountain belt revealed by the trace element rhenium. *Earth and Planetary Science Letters*, 403, 27–36. <https://doi.org/10.1016/j.epsl.2014.06.021>
- Hilton, R. G., Galy, A., & Hovius, N. (2008). Riverine particulate organic carbon from an active mountain belt: Importance of landslides. *Global Biogeochemical Cycles*, 22(1), 1–12. <https://doi.org/10.1029/2006GB002905>
- Hilton, R. G., Galy, A., Hovius, N., Horng, M., & Chen, H. (2011). Efficient transport of fossil organic carbon to the ocean by steep mountain rivers: An orogenic carbon sequestration mechanism. *Geology*, 39(1), 71–74. <https://doi.org/10.1130/G31352.1>
- Hilton, R. G., Galy, A., Hovius, N., Horng, M. J., & Chen, H. (2010). The isotopic composition of particulate organic carbon in mountain rivers of Taiwan. *Geochimica et Cosmochimica Acta*, 74(11), 3164–3181. <https://doi.org/10.1016/j.gca.2010.03.004>
- Hilton, R. G., Galy, V., Gaillardet, J., Dellinger, M., Bryant, C., O'Regan, M., et al. (2015). Erosion of organic carbon in the Arctic as a geological carbon dioxide sink. *Nature*, 524(7563), 84–87. <https://doi.org/10.1038/nature14653>
- Hilton, R. G., & West, A. J. (2020). Mountains, erosion and the carbon cycle. *Nature Reviews Earth & Environment*, 1(6), 284–299. <https://doi.org/10.1038/s43017-020-0058-6>
- Hollingsworth, E. H. (2023). Spatial and temporal patterns in petrogenic organic carbon mobilisation during the Paleocene-Eocene Thermal Maximum [Dataset]. <https://doi.org/10.17605/OSF.IO/F8HJC>
- Inglis, G. N., Bragg, F., Burls, N. J., Cramwinckel, M. J., Evans, D., Foster, G. L., et al. (2020). Global mean surface temperature and climate sensitivity of the early Eocene Climatic Optimum (EECO), Paleocene-Eocene Thermal Maximum (PETM), and latest Paleocene. *Climate of the Past*, 16(5), 1953–1968. <https://doi.org/10.5194/cp-16-1953-2020>
- Inglis, G. N., Naafs, B. D. A., Zheng, Y., McClymont, E. L., Evershed, R. P., & Pancost, R. D. (2018). Distributions of geohopanoids in peat: Implications for the use of hopanoid-based proxies in natural archives. *Geochimica et Cosmochimica Acta*, 224, 249–261. <https://doi.org/10.1016/j.gca.2017.12.029>
- Jiang, J., Hu, X., Li, J., Garzanti, E., Jiang, S., Cui, Y., & Wang, Y. (2023). Eustatic change across the Paleocene-Eocene Thermal Maximum in the epicontinental Tarim seaway. *Global and Planetary Change*, 229, 104241. <https://doi.org/10.1016/j.gloplacha.2023.104241>
- John, C. M., Banerjee, N. R., Longstaffe, F. J., Sica, C., Law, K. R., & Zachos, J. C. (2012). Clay assemblage and oxygen isotopic constraints on the weathering response to the Paleocene-Eocene Thermal Maximum, East Coast of North America. *Geology*, 40(7), 591–594. <https://doi.org/10.1130/G32785.1>
- John, C. M., Bohaty, S. M., Zachos, J. C., Sluijs, A., Gibbs, S., Brinkhuis, H., & Bralower, T. J. (2008). North American continental margin records of the Paleocene-Eocene Thermal Maximum: Implications for global carbon and hydrological cycling. *Paleoceanography*, 23(2), 1–20. <https://doi.org/10.1029/2007PA001465>
- Jones, M. T., Percival, L. M. E., Stokke, E. W., Frieling, J., Mather, T. A., Riber, L., et al. (2019). Mercury anomalies across the Palaeocene-Eocene Thermal Maximum. *Climate of the Past*, 15(1), 217–236. <https://doi.org/10.5194/cp-15-217-2019>
- Kaiho, K., Arinobu, T., Ishiwatari, R., Morgans, H. E. G., Okada, H., Takeda, N., et al. (1996). Latest Paleocene benthic foraminiferal extinction and environmental changes at Tawanui, New Zealand. *Paleoceanography*, 11(4), 447–465. <https://doi.org/10.1029/96PA01021>
- Kao, S. J., Dai, M. H., Wei, K. Y., Blair, N. E., & Lyons, W. B. (2008). Enhanced supply of fossil organic carbon to the Okinawa trough since the last deglaciation. *Paleoceanography*, 23(2), 1–10. <https://doi.org/10.1029/2007PA001440>
- Kao, S. J., Hilton, R. G., Selvaraj, K., Dai, M., Zehetner, F., Huang, J. C., et al. (2014). Preservation of terrestrial organic carbon in marine sediments offshore Taiwan: Mountain building and atmospheric carbon dioxide sequestration. *Earth Surface Dynamics*, 2(1), 127–139. <https://doi.org/10.5194/esurf-2-127-2014>
- Kaya, M. Y., Dupont-Nivet, G., Frieling, J., Fioroni, C., Rohmann, A., Altner, S. Ö., et al. (2022). The Eurasian epicontinental sea was an important carbon sink during the Palaeocene-Eocene Thermal Maximum. *Communications Earth and Environment*, 3(1), 1–10. <https://doi.org/10.1038/s43247-022-00451-4>
- Kiehl, J. T., Zarzycki, C. M., Shields, C. A., & Rothstein, M. V. (2021). Simulated changes to tropical cyclones across the Paleocene-Eocene Thermal Maximum (PETM) boundary. *Palaeogeography, Palaeoclimatology, Palaeoecology*, 572, 110421. <https://doi.org/10.1016/j.palaeo.2021.110421>
- Kirtland Turner, S. (2018). Constraints on the onset duration of the Paleocene-Eocene Thermal Maximum. *Philosophical Transactions of the Royal Society A*, 376(2130), 1–16. <https://doi.org/10.1098/rsta.2017.0082>
- Kopp, R. E., Schumann, D., Raub, T. D., Powars, D. S., Godfrey, L. V., Swanson-Hysell, N. L., et al. (2009). An Appalachian Amazon? Magnetofossil evidence for the development of a tropical river-like system in the mid-Atlantic United States during the Paleocene-Eocene Thermal Maximum. *Paleoceanography*, 24(4), 1–17. <https://doi.org/10.1029/2009PA001783>
- Korasidis, V. A., Wing, S. L., Shields, C. A., & Kiehl, J. T. (2022). Global changes in terrestrial vegetation and continental climate during the Paleocene-Eocene Thermal Maximum. *Paleoceanography and Paleoclimatology*, 37(4), 1–21. <https://doi.org/10.1029/2021PA004325>

- Kraus, M. J., McInerney, F. A., Wing, S. L., Secord, R., Baczynski, A. A., & Bloch, J. I. (2013). Paleohydrologic response to continental warming during the Paleocene-Eocene Thermal Maximum, Bighorn Basin, Wyoming. *Palaeoogeography, Palaeoecology, Palaeoecology*, 370, 196–208. <https://doi.org/10.1016/j.palaeo.2012.12.008>
- Kraus, M. J., & Riggins, S. (2007). Transient drying during the Paleocene-Eocene Thermal Maximum (PETM): Analysis of paleosols in the bighorn basin, Wyoming. *Palaeoogeography, Palaeoecology, Palaeoecology*, 245(3–4), 444–461. <https://doi.org/10.1016/j.palaeo.2006.09.011>
- Kurtz, A. C., Kump, L. R., Arthur, M. A., Zachos, J. C., & Paytan, A. (2003). Early Cenozoic decoupling of the global carbon and sulfur cycles. *Paleoceanography*, 18(4), 1–14. <https://doi.org/10.1029/2003PA000908>
- Kusch, S., & Rush, D. (2022). Revisiting the precursors of the most abundant natural products on Earth: A look back at 30+ years of bacteriohopanepolyol (BHP) research and ahead to new frontiers. *Organic Geochemistry*, 172, 104469. <https://doi.org/10.1016/j.orggeochem.2022.104469>
- Lee, J.-Y., Marotzke, J., Bala, G., Cao, L., Corti, S., Dunne, J. P., et al. (2021). Future global climate: Scenario-based projections and near-term information coordinating. In V. Masson-Delmotte, P. Zhai, A. Pirani, S. L. Connors, C. Péan, S. Berger, et al. (Eds.), *Climate change 2021: The physical science basis. Contribution of working group I to the sixth assessment report of the intergovernmental panel on climate change*. Cambridge University Press. <https://doi.org/10.1017/9781009157896.006.553>
- Leithold, E. L., Blair, N. E., & Perkey, D. W. (2006). Geomorphologic controls on the age of particulate organic carbon from small mountainous and upland rivers. *Global Biogeochemical Cycles*, 20(3), 1–11. <https://doi.org/10.1029/2005GB002677>
- Li, J., Hu, X., Zachos, J. C., Garzanti, E., & BouDagher-Fadel, M. (2020). Sea level, biotic and carbon-isotope response to the Paleocene-Eocene Thermal Maximum in Tibetan Himalayan platform carbonates. *Global and Planetary Change*, 194, 103316. <https://doi.org/10.1016/j.gloplacha.2020.103316>
- Lyons, S. L., Baczynski, A. A., Babila, T. L., Bralower, T. J., Hajek, E. A., Kump, L. R., et al. (2019). Paleocene-Eocene Thermal Maximum prolonged by fossil carbon oxidation. *Nature Geoscience*, 12(1), 54–60. <https://doi.org/10.1038/s41561-018-0277-3>
- Lyster, S. J., Whittaker, A. C., Allison, P. A., Lunt, D. J., & Farnsworth, A. (2020). Predicting sediment discharges and erosion rates in deep time—Examples from the late Cretaceous North American continent. *Basin Research*, 32(6), 1547–1573. <https://doi.org/10.1111/bre.12442>
- Ma, Z., Gray, E., Thomas, E., Murphy, B., Zachos, J., & Paytan, A. (2014). Carbon sequestration during the Paleocene-Eocene Thermal Maximum by an efficient biological pump. *Nature Geoscience*, 7(5), 382–388. <https://doi.org/10.1038/ngeo2139>
- Mackenzie, A. S., Patience, R. L., Maxwell, J. R., Vandenbroucke, M., & Durand, B. (1980). Molecular parameters of maturation in the Toarcian shales, Paris Basin, France—I. Changes in the configurations of acyclic isoprenoid alkanes, steranes and triterpanes. *Geochimica et Cosmochimica Acta*, 44(11), 1709–1721. [https://doi.org/10.1016/0016-7037\(80\)90222-7](https://doi.org/10.1016/0016-7037(80)90222-7)
- McInerney, F. A., & Wing, S. L. (2011). The Paleocene-Eocene Thermal Maximum: A perturbation of carbon cycle, climate, and biosphere with implications for the future. *Annual Review of Earth and Planetary Sciences*, 39(1), 489–516. <https://doi.org/10.1146/annurev-earth-040610-133431>
- Meyers, S. R. (2014). Astrochron: An R package for astrochronology. Retrieved from <https://cran.r-project.org/package=astrochron>
- Murphy, B. H., Farley, K. A., & Zachos, J. C. (2010). An extraterrestrial ³H₂-based timescale for the Paleocene-Eocene Thermal Maximum (PETM) from Walvis Ridge, IODP Site 1266. *Geochimica et Cosmochimica Acta*, 74(17), 5098–5108. <https://doi.org/10.1016/j.gca.2010.03.039>
- Pagani, M., Pedentchouk, N., Huber, M., Sluijs, A., Schouten, S., Brinkhuis, H., et al. (2006). Arctic hydrology during global warming at the Paleocene/Eocene Thermal Maximum. *Nature*, 442(7103), 671–675. <https://doi.org/10.1038/nature05043>
- Pancost, R. D., Coleman, J. M., Love, G. D., Chatzi, A., Bouloubassi, I., & Snape, C. E. (2008). Kerogen-bound glycerol dialkyl tetraether lipids released by hydrolysis of marine sediments: A bias against incorporation of sedimentary organisms? *Organic Geochemistry*, 39(9), 1359–1371. <https://doi.org/10.1016/j.orggeochem.2008.05.002>
- Papadomanolaki, N. M., Sluijs, A., & Slomp, C. P. (2022). Eutrophication and deoxygenation forcing of marginal marine Organic carbon burial during the PETM. *Paleoceanography and Paleoclimatology*, 37(3), 1–23. <https://doi.org/10.1029/2021PA004232>
- Penman, D. E., Hönisch, B., Zeebe, R. E., Thomas, E., & Zachos, J. C. (2014). Rapid and sustained surface ocean acidification during the Paleocene-Eocene Thermal Maximum. *Paleoceanography*, 29(5), 357–369. <https://doi.org/10.1002/2014PA002621>
- Peters, K. E., Walters, C. C., & Moldovan, J. M. (2005). *The biomarker guide* (Vol. 1). Cambridge University Press.
- Petsch, S. T., Berner, R. A., & Eglinton, T. I. (2000). A field study of the chemical weathering of ancient sedimentary organic matter. *Organic Geochemistry*, 31(5), 475–487. [https://doi.org/10.1016/S0146-6380\(00\)00014-0](https://doi.org/10.1016/S0146-6380(00)00014-0)
- Pogge von Strandmann, P. A. E., Jones, M. T., Joshua West, A., Murphy, M. J., Stokke, E. W., Tarbuck, G., et al. (2021). Lithium isotope evidence for enhanced weathering and erosion during the Paleocene-Eocene Thermal Maximum. *Science Advances*, 7(42), 1–12. <https://doi.org/10.1126/sciadv.abh4224>
- Polik, C. A., Elling, F. J., & Pearson, A. (2018). Impacts of Paleoecology on the TEX 86 sea surface temperature proxy in the Pliocene-Pleistocene Mediterranean Sea. *Paleoceanography and Paleoclimatology*, 33(12), 1472–1489. <https://doi.org/10.1029/2018PA003494>
- Robert, C., & Kennett, J. P. (1994). Antarctic subtropical humid episode at the Paleocene-Eocene boundary: Clay-mineral evidence. *Geology*, 22(3), 211–214. [https://doi.org/10.1130/0091-7613\(1994\)022<0211:ASHEAT>2.3.CO;2](https://doi.org/10.1130/0091-7613(1994)022<0211:ASHEAT>2.3.CO;2)
- Röhl, U., Westerhold, T., Bralower, T. J., & Zachos, J. C. (2007). On the duration of the Paleocene-Eocene Thermal Maximum (PETM). *Geochemistry, Geophysics, Geosystems*, 8(12), 1–13. <https://doi.org/10.1029/2007GC001784>
- Rosa-Putra, S., Nalin, R., Domenach, A. M., & Rohmer, M. (2001). Novel hopanoids from *Frankia* spp. and related soil bacteria: Squalene cyclization and significance of geological biomarkers revisited. *European Journal of Biochemistry*, 268(15), 4300–4306. <https://doi.org/10.1046/j.1432-1327.2001.02348.x>
- Rush, W. D., Kiehl, J. T., Shields, C. A., & Zachos, J. C. (2021). Increased frequency of extreme precipitation events in the North Atlantic during the PETM: Observations and theory. *Palaeoogeography, Palaeoecology, Palaeoecology*, 568, 110289. <https://doi.org/10.1016/j.palaeo.2021.110289>
- Schmitz, B., & Pujalte, V. (2003). Sea-level, humidity, and land-erosion records across the initial Eocene thermal maximum from a continental-marine transect in northern Spain. *Geology*, 31(8), 689–692. <https://doi.org/10.1130/G19527.1>
- Schmitz, B., & Pujalte, V. (2007). Abrupt increase in seasonal extreme precipitation at the Paleocene-Eocene boundary. *Geology*, 35(3), 215–218. <https://doi.org/10.1130/G23261A.1>
- Self-Trail, J. M., Robinson, M. M., Bralower, T. J., Sessa, J. A., Hajek, E. A., Kump, L. R., et al. (2017). Shallow marine response to global climate change during the Paleocene-Eocene Thermal Maximum, Salisbury Embayment, USA. *Paleoceanography*, 32(7), 710–728. <https://doi.org/10.1002/2017PA003096>
- Shcherbinina, E., Gavrilov, Y., Iakovleva, A., Pokrovsky, B., Golovanova, O., & Aleksandrova, G. (2016). Environmental dynamics during the Paleocene-Eocene Thermal Maximum (PETM) in the northeastern Peri-Tethys revealed by high-resolution micropaleontological and geochemical studies of a Caucasian key section. *Palaeoogeography, Palaeoecology, Palaeoecology*, 456, 60–81. <https://doi.org/10.1016/j.palaeo.2016.05.006>

- Shields, C. A., Kiehl, J. T., Rush, W., Rothstein, M., & Snyder, M. A. (2021). Atmospheric rivers in high-resolution simulations of the Paleocene Eocene Thermal Maximum (PETM). *Palaeogeography, Palaeoclimatology, Palaeoecology*, 567, 110293. <https://doi.org/10.1016/j.palaeo.2021.110293>
- Sluijs, A., Bijl, P. K., Schouten, S., Röhl, U., Reichert, G.-J., & Brinkhuis, H. (2011). Southern ocean warming, sea level and hydrological change during the Paleocene-Eocene Thermal Maximum. *Climate of the Past*, 7(1), 47–61. <https://doi.org/10.5194/cp-7-47-2011>
- Sluijs, A., & Brinkhuis, H. (2009). A dynamic climate and ecosystem state during the Paleocene-Eocene Thermal Maximum: Inferences from dinoflagellate cyst assemblages on the New Jersey Shelf. *Biogeosciences*, 6(8), 1755–1781. <https://doi.org/10.5194/bg-6-1755-2009>
- Sluijs, A., Brinkhuis, H., Crouch, E. M., John, C. M., Handley, L., Munsterman, D., et al. (2008). Eustatic variations during the Paleocene-Eocene greenhouse world. *Paleoceanography*, 23(4), 1–18. <https://doi.org/10.1029/2008PA001615>
- Sluijs, A., Frieling, J., Inglis, G. N., Nierop, K. G. J., Peterse, F., Sangiorgi, F., & Schouten, S. (2020). Late Paleocene–early Eocene Arctic Ocean sea surface temperatures: Reassessing biomarker paleothermometry at Lomonosov Ridge. *Climate of the Past*, 16(6), 2381–2400. <https://doi.org/10.5194/cp-16-2381-2020>
- Sluijs, A., Röhl, U., Schouten, S., Brumsack, H.-I., Sangiorgi, F., Sinninghe Damsté, J. S., & Brinkhuis, H. (2008). Arctic late Paleocene–early Eocene paleoenvironments with special emphasis on the Paleocene-Eocene Thermal Maximum (Lomonosov Ridge, Integrated ocean drilling program expedition 302). *Paleoceanography*, 23(1), 1–17. <https://doi.org/10.1029/2007PA001495>
- Sluijs, A., Schouten, S., Pagani, M., Woltering, M., Brinkhuis, H., Dickens, G. R., et al. (2006). Subtropical Arctic Ocean temperatures during the Paleocene/Eocene Thermal Maximum. *Nature*, 441(1), 610–613. <https://doi.org/10.1038/nature04668>
- Sluijs, A., van Roij, L., Harrington, G. J., Schouten, S., Sessa, J. A., Levay, L. J., et al. (2014). Warming, euxinia and sea level rise during the Paleocene-Eocene Thermal Maximum on the Gulf Coastal Plain: Implications for ocean oxygenation and nutrient cycling. *Climate of the Past*, 10(4), 1421–1439. <https://doi.org/10.5194/cp-10-1421-2014>
- Smith, J. C., Galy, A., Hovius, N., Tye, A. M., Turowski, J. M., & Schleppli, P. (2013). Runoff-driven export of particulate organic carbon from soil in temperate forested uplands. *Earth and Planetary Science Letters*, 365, 198–208. <https://doi.org/10.1016/j.epsl.2013.01.027>
- Sparkes, R. B., Maher, M., Blewett, J., Selver, A. O., Gustafsson, O., Semiletov, I. P., & Van Dongen, B. E. (2018). Carbonaceous material export from Siberian permafrost tracked across the Arctic Shelf using Raman spectroscopy. *The Cryosphere*, 12(10), 3293–3309. <https://doi.org/10.5194/tc-12-3293-2018>
- Stallard, R. F. (1998). Terrestrial sedimentation and the carbon cycle: Coupling weathering and erosion to carbon burial. *Global Biogeochemical Cycles*, 12(2), 231–257. <https://doi.org/10.1029/98GB00741>
- Stassen, P., Thomas, E., & Speijer, R. P. (2012). Integrated stratigraphy of the Paleocene-Eocene Thermal Maximum in the New Jersey Coastal Plain: Toward understanding the effects of global warming in a shelf environment. *Paleoceanography*, 27(4), 1–17. <https://doi.org/10.1029/2012PA002323>
- Storey, M., Duncan, R. A., & Swisher, C. C. (2007). Paleocene-Eocene Thermal Maximum and the opening of the northeast Atlantic. *Science*, 316(5824), 587–589. <https://doi.org/10.1126/science.1135274>
- Svensen, H., Planke, S., Maithe-Sørensen, A., Jamtveit, B., Myklebust, R., Eidem, T. R., & Rey, S. S. (2004). Release of methane from a volcanic basin as a mechanism for initial Eocene global warming. *Nature*, 429(6991), 542–545. <https://doi.org/10.1038/nature02566>
- Tierney, J. E., Zhu, J., Li, M., Ridgwell, A., Hakim, G. J., Poulsen, C. J., et al. (2022). Spatial patterns of climate change across the Paleocene–Eocene Thermal Maximum. *Proceedings of the National Academy of Sciences of the United States of America*, 119(42), 1–7. <https://doi.org/10.1073/pnas.2205326119>
- Walker, J. C. G., Hays, P. B., & Kasting, J. F. (1981). A negative feedback mechanism for the long-term stabilization of Earth's surface temperature. *Journal of Geophysical Research*, 86(10), 9776–9782. <https://doi.org/10.1029/JC086iC10p09776>
- Willard, D. A., Donders, T. H., Reichgelt, T., Greenwood, D. R., Sangiorgi, F., Peterse, F., et al. (2019). Arctic vegetation, temperature, and hydrology during early Eocene transient global warming events. *Global and Planetary Change*, 178, 139–152. <https://doi.org/10.1016/j.gloplacha.2019.04.012>
- Winguth, A., Shellito, C., Shields, C., & Winguth, C. (2010). Climate response at the Paleocene-Eocene Thermal Maximum to greenhouse gas forcing—a model study with CCSM3. *Journal of Climate*, 23(10), 2562–2584. <https://doi.org/10.1175/2009JCLI3113.1>
- Zeebe, R. E. (2013). What caused the long duration of the Paleocene-Eocene Thermal Maximum. *Paleoceanography*, 28(3), 440–452. <https://doi.org/10.1002/palo.20039>
- Zeebe, R. E., Dickens, G. R., Ridgwell, A., Sluijs, A., & Thomas, E. (2014). Onset of carbon isotope excursion at the Paleocene-Eocene Thermal Maximum took millennia, not 13 years. *Proceedings of the National Academy of Sciences of the United States of America*, 111(12), 1062–1063. <https://doi.org/10.1073/pnas.1321177111>
- Zeebe, R. E., & Lourens, L. J. (2019). Solar system chaos and the Paleocene–Eocene boundary age constrained by geology and astronomy. *Science*, 364(6456), 926–929. <https://doi.org/10.1126/science.aax0612>
- Zeebe, R. E., Zachos, J. C., & Dickens, G. R. (2009). Carbon dioxide forcing alone insufficient to explain Paleocene-Eocene Thermal Maximum warming. *Nature Geoscience*, 2(8), 576–580. <https://doi.org/10.1038/ngeo578>

References From the Supporting Information

- Bralower, T. J., Kump, L. R., Self-Trail, J. M., Robinson, M. M., Lyons, S., Babila, T., et al. (2018). Evidence for shelf acidification during the onset of the Paleocene-Eocene Thermal Maximum. *Paleoceanography and Paleoclimatology*, 33(12), 1408–1426. <https://doi.org/10.1029/2018PA003382>
- Gavrilov, Y. O., Shcherbinina, E. A., & Oberhänsli, H. (2003). Paleocene-Eocene boundary events in the northeastern Peri-Tethys. *Special Paper of the Geological Society of America*, 369, 147–168. <https://doi.org/10.1130/0-8137-2369-8.147>
- Harris, A. D., Miller, K. G., Browning, J. V., Sugarman, P. J., Olsson, R. K., Cramer, B. S., & Wright, J. D. (2010). Integrated stratigraphic studies of Paleocene-lowermost Eocene sequences, New Jersey Coastal Plain: Evidence for glacioeustatic control. *Paleoceanography*, 25(3), 1–18. <https://doi.org/10.1029/2009PA001800>
- Hollis, C. J., Dunkley Jones, T., Anagnostou, E., Bijl, P. K., Cramwinckel, M. J., Cui, Y., et al. (2019). The DeepMIP contribution to PMIP4: Methodologies for selection, compilation and analysis of latest Paleocene and early Eocene climate proxy data, incorporating version 0.1 of the DeepMIP database. *Geoscientific Model Development*, 12(7), 3149–3206. <https://doi.org/10.5194/gmd-12-3149-2019>
- Junium, C. K., Dickson, A. J., & Uveges, B. T. (2018). Perturbation to the nitrogen cycle during rapid early Eocene global warming. *Nature Communications*, 9(1), 3186. <https://doi.org/10.1038/s41467-018-05486-w>

- Nicholas, C. J., Pearson, P. N., Bown, P. R., Jones, T. D., Huber, B. T., Karega, A., et al. (2006). Stratigraphy and sedimentology of the Upper Cretaceous to Paleogene Kilwa Group, southern coastal Tanzania. *Journal of African Earth Sciences*, 45(4–5), 431–466. <https://doi.org/10.1016/j.jafrearsci.2006.04.003>
- Self-Trail, J. M., Powars, D. S., Watkins, D. K., & Wandless, G. A. (2012). Calcareous nannofossil assemblage changes across the Paleocene-Eocene Thermal Maximum: Evidence from a shelf setting. *Marine Micropaleontology*, 92(93), 61–80. <https://doi.org/10.1016/j.marmicro.2012.05.003>